Wide Range X-Ray to Infrared Photon Detection and Energy Storage in $LiTaO_3:Bi^{3+},Dy^{3+}$ Perovskite

Lyu, Tianshuai; Dorenbos, Pieter; Li, Canhua; Wei, Zhanhua

DOI
10.1002/lpor.202200055

Publication date
2022

Document Version
Final published version

Published in
Laser and Photonics Reviews

LASER & PHOTONICS REVIEWS

www.lpr-journal.org

Wide Range X-Ray to Infrared Photon Detection and Energy Storage in $LiTaO_3:Bi^{3+},Dy^{3+}$ Perovskite

Tianshuai Lyu, Pieter Dorenbos, Canhua Li, and Zhanhua Wei**

It is challenging to obtain a material that can detect photons ranging from X-rays to infrared light. Such materials have promising use to develop advanced applications like in information storage, anticounterfeiting, or X-ray imaging. This article reports on such a material; $LiTaO_3:xBi^{3+},yDy^{3+}$ perovskite phosphor. Experimental spectroscopy, thermoluminescence, and vacuum referred binding energy diagram (VRBE) construction are combined to study the trapping processes of charge carriers. The VRBEs in the ground or excited states of Bi^{3+} and Bi^{2+} are discussed. Bi^{3+} emerges to act as a ≈1.3 eV deep hole capturing center and it may possibly also act as a 0.80 ± 0.5 eV deep electron trapping center. A linear relation between the amount of stored charge carriers and a photochromic phenomenon both induced by X-rays or 254 nm UV-light charging appears. The stored charge carriers in $LiTaO_3:xBi^{3+},yDy^{3+}$ are removed by heating or with an optically stimulated process with 365 nm UV light to 850 nm infrared laser. More than 3 or 40 h of Bi^{3+} and Dy^{3+} based white afterglow is measurable in $LiTaO_3:0.005Bi^{3+},0.004Dy^{3+}$ after exposure to X-rays or 254 nm UV light. Proof-of-concept light detection applications like 2D information storage and anticounterfeiting or X-ray imaging are demonstrated by using the phtotochromic and white afterglow $LiTaO_3:xBi^{3+},yDy^{3+}$ phosphors.

1. Introduction

Photochromism is an optically induced color change phenomenon.[1] Under light stimulation, a defect in a compound can change from its initial state to a different state, which results in a different absorption spectrum.[2] For some compounds, the defect in a different state can reversibly change back to its initial state upon electrical, thermal, or optical stimulation. Because of this feature, a photochromic phosphor has application in optical sensing like smart color tailorable window, optical data storage,[3] information anticounterfeiting and display.[2,4] Particularly, the luminescence property of a luminescence center in a photochromic compound can be tailored for optical storage memory application.[3] Organic compounds have widely been studied to explore photochromic materials, and some organic compounds like diarylethene with good photochromic contrast have been reported.[5] However, organic photochromic compounds have some intrinsic problems like poor thermal stability, poor chemical stability in moisture atmosphere, short lifetime, and difficult synthesis procedure with the use of highly toxic chemicals.[5] These drawbacks lead to difficulty in developing organic photochromic compounds for commercial applications. In contrast, inorganic photochromic compounds normally show a facile synthesis procedure, long lifetime, good chemical and thermal stability. Therefore, there is an interest in developing inorganic photochromic compounds.[4] To date, well-known examples are $WO_3:Yb^{3+},Er^{3+}$,[6] $PbWO_4:Yb^{3+},Er^{3+}$,[7] $CaWO_4:Yb^{3+},Er^{3+}$,[8] $CaSnO_4:Eu$,[9] $K_{0.5}Na_{0.5}NbO_3:Eu$,[1] and lanthanide-doped $BaMgSiO_4$.[10] Transition-metal-based compounds often have a long photochromic response time with poor reversibility of photochromism. For instance, it takes more than 0.5 h to observe the photochromic phenomenon in TiO_2,[11] and the reversible photochromic phenomenon cannot be reproduced in MoO_3 after thermal bleaching.[12] For some ferroelectric ceramics like $(K_{0.5}Na_{0.5})NbO_3:Tb^{3+}$, the reversible photochromism is realized after first exposure to 407 nm light for 20 s followed by thermal bleaching at 423 K with a duration of 10 s.[13] Compared with thermal, moist, or mechanical bleaching, optical bleaching has superior advantages because the light can be easily and precisely tailored for developing advanced optical-sensing applications. However, there are rare reports studying the effect of a wide energy range of photons from X-rays to infrared light on the formation of photochromism in inorganic compounds. Currently, a scientific and effective methodology has not been established to guide the design of optically induced photochromism in inorganic compounds. Therefore, it is challenging to design and realize reversible photochromism in inorganic compounds after only exposure to different energy photon stimulation from X-rays to infrared light.

T. Lyu, C. Li, Z. Wei
Xiamen Key Laboratory of Optoelectronic Materials and Advanced Manufacturing
Institute of Luminescent Materials and Information Displays, College of Materials Science and Engineering
Huaqiao University
Xiamen 361021, China
E-mail: lv_tianshuai@hqu.edu.cn; lv_tianshuai@126.com; weizhanhua@hqu.edu.cn

P. Dorenbos
Delft University of Technology
Faculty of Applied Sciences, Department of Radiation Science and Technology
Mekelweg 15, Delft 2629JB, The Netherlands

DOI: 10.1002/lpor.202200055

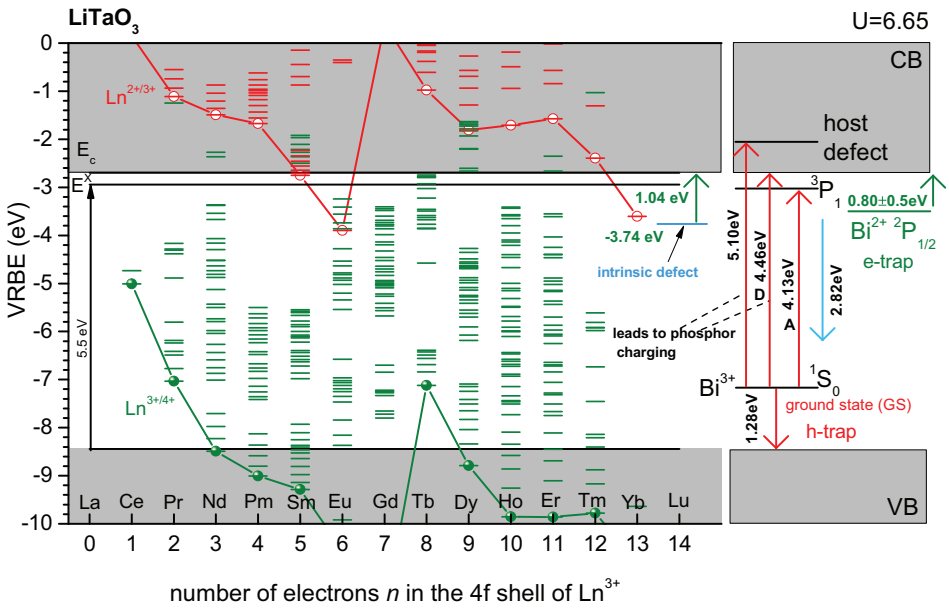

Figure 1. Vacuum referred binding energy (VRBE) diagram for $LiTaO_3$ including the energy level locations of lanthanides, divalent and trivalent bismuth. $Ln^{2+/3+}$ and $Ln^{3+/4+}$ curves connect the binding energies in the ground states of divalent and trivalent lanthanides. E_c and E_X are the binding energies at the conduction band (CB) bottom and in the host exciton state. The VRBEs in the $^1S_0$ ground state and the $^3P_1$ excited state of Bi^{3+}, and the Bi^{3+}→CB metal-to-metal charge-transfer (MMCT) band (D-band) are illustrated. Solid arrows indicate experimentally observed transitions.

Afterglow phosphors, also named persistent luminescence materials, are known as compounds that can show a sustained photon emission with a duration of few minutes to hours after stopping excitation.[14] Because of this property, afterglow phosphors have many applications in light sensing like battery-free light dosimeter[15] and imaging.[16] Currently, many afterglow phosphors emitting in the blue or green region have been reported.[17] Red afterglow was recently reported in $SrLiAl_3N_4$:Eu^{2+} after 254 nm UV-light charging.[18] However, there are rare reports on white afterglow phosphors after X-rays or UV-light charging.[19] There are several unique properties of white afterglow phosphors for developing advanced light-sensing applications. For example, the maximum eye sensitivity curve is covered by a white afterglow phosphor. A substance can be seen correctly under illumination from a white afterglow phosphor in the dark,[19,20] which is unique for illumination[20a] and anticounterfeiting applications in the dark.[21] To the best of our knowledge, there is no report on a phosphor that combines X-rays or UV-light-induced white persistent luminescence with the photochromic phenomenon for optical-sensing applications.

Lithium tantalate ($LiTaO_3$) crystallizes at room temperature (RT) in a perovskite structure with trigonal phase and an *R3c* space group. $LiTaO_3$ crystals combine unique features like piezoelectric, pyroelectric, and luminescence properties, leading to fascinating applications like in nonlinear optics and infrared sensors.[22] $LiTaO_3$ crystal has also a high density of ≈7.45 g cm^{-3}, which provides it with a high absorption coefficient for X-rays. Tb^{3+}-doped $LiTaO_3$ has been studied in 1996 for X-ray charged storage phosphor application.[23] In 2020, Bi^{3+}-doped $LiTaO_3$ has been studied for persistent luminescence phosphor applications by Hu et al. in ref. [24]. The bismuth atom has a $[Xe]4f^{14}5d^{10}6s^26p^3$ configuration. Different valence states of bismuth can be generated when different outermost electrons of the bismuth atom are removed, for instance, Bi^{2+} (the outermost electron is $6p^1$), Bi^{3+} ($6s^2$), or Bi^{4+} ($6s^1$). In an inorganic compound, a Bi^{3+} cation can capture an electron to form Bi^{2+} and also can capture a hole to form Bi^{4+}. The dual role of trivalent bismuth as an electron or hole-capturing center has been studied in $REPO_4$[25] and $ARE(Si,Ge)O_4$ (A = Li and Na; RE = Y, Lu).[16] The charge-carrier capturing and detrapping processes in bismuth and/or lanthanide-doped $LiTaO_3$ still remain unknown.

The objective of this work is to explore and systematically study trivalent bismuth- and/or dysprosium-doped $LiTaO_3$, which combines white persistent luminescence with a reversible photochromic phenomenon. We will demonstrate that this smart sensing material can detect a wide energy range of photons from X-rays to 850 nm infrared light. To understand the sensing material, thermoluminescence (TL), photoluminescence at 10 K and RT, reflectivity spectra, and vacuum-referred binding energy (VRBE) diagram construction have been combined, and the charge-carrier capturing and release processes in $LiTaO_3$:xBi^{3+},yDy^{3+} have been studied. **Figure 1** shows the vacuum referred binding energy diagram for the lanthanides in $LiTaO_3$ as obtained in ref. [26]. In this work, we will discuss the VRBEs in the ground and excited states of Bi^{3+} and Bi^{2+}, and demonstrate that intrinsic defects act as the electron-capturing centers, while Bi^{3+} acts as a hole-capturing and recombination center in $LiTaO_3$:xBi^{3+},yDy^{3+}. Dy^{3+} can, according to the diagram, trap neither an electron nor a hole. It will act as a luminescence center to assist in generating white luminescence and afterglow. More than 40 h white persistent luminescence is measurable in the optimized composition $LiTaO_3$:$0.005Bi^{3+}$,$0.004Dy^{3+}$ after 254 nm UV-light charging. We will show proof-of-concept 2D information storage, display, or X-ray imaging by using the developed $LiTaO_3$:xBi^{3+},yDy^{3+}-sensing materials.

2. Experimental Section

The supplier was Shanghai Macklin Biochemical Co., Ltd. for the starting chemical Li_2CO_3 (99.99%) and Shanghai Aladdin chemical company for other starting chemicals used in this work. All starting chemicals were stored in a dry room and used without further treatment. The $LiTaO_3$:xBi^{3+},yDy^{3+} compounds were synthesized by using a high-temperature solid state reaction method. The appropriate stoichiometric mixture of Li_2CO_3 (99.99%), Ta_2O_5 (99.99%), Bi_2O_3 (99.99%), and Dy_2O_3 (99.99%) was mixed well in an agate mortar for ≈20 min with the help of acetone solution. After drying in air, the mixed powder was transferred from the agate mortar to a covered alumina crucible, which was then heated at 1250 °C for a duration of 6 h in a tube oven under ambient atmosphere. The utilized heating rate for the oven was 3 °C min^{-1}. After sintering at 1250 °C, the synthesized compounds were naturally cooled to RT and mixed homogeneously again in an agate mortar before further measurements. To optimize the photochromic phosphors, the $LiTaO_3$:xBi^{3+},yDy^{3+} compounds were also synthesized at 1300, 1350, and 1400 °C with a duration of 6 h. A $LiTaO_3$:0.005Bi^{3+},0.001Dy^{3+} pill was also prepared, which was heated at 1300 or 1350 °C with a duration of 6 h.

The crystal structures of all the synthesized $LiTaO_3$:xBi^{3+},yDy^{3+} compounds were identified at RT by a Japan Rigaku Smar/SmartLa X-ray diffraction setup. The setup contained a water-cooled X-ray tube that operates at 40 kV and 30 mA, resulting in the characteristic Cu Kα radiation with a wavelength of $\lambda = 0.15405$ nm. To check whether the crystal structure of the photochromic $LiTaO_3$:0.002Bi^{2+},0.004Dy^{3+} was changed or not after exposure to 254 nm UV light, the X-ray diffraction patterns (XRD) patterns were recorded for $LiTaO_3$:0.002Bi^{2+},0.004Dy^{3+} without 254 nm UV-light illumination and after exposure to 254 nm UV light with a duration of 60 s at RT in the dark.

A Japan JEOL JSM-7610FPlus electron microscope was utilized to record the scanning electron microscope (SEM) images and the energy dispersive X-ray spectroscopy (EDX) mappings. To analyze the optical properties of the as-prepared compounds, photoluminescence excitation spectra (PLE), emission spectra (PL), persistence luminescence spectra at RT, and RT isothermal decay curves were recorded by utilizing an FLS920 fluorescence spectrometer (Edinburgh Instruments, Ltd.). This spectrometer was equipped with a single photon-counting photomultiplier (PMT, Hamamatsu, R928P), an Xe900 continuous xenon lamp, and a monochromator. During optical measurements, the R928P photomultiplier was cooled to ≈253 K in order to efficiently detect the emission from 200 to ≈870 nm with high signal-to-background ratio. The measured photoluminescence excitation and emission spectra were corrected using the wavelength-dependent excitation intensity of the Xe900 continuous xenon lamp. Photoluminescence excitation and emission spectra at 10 K were measured by an FLS980 fluorescence spectrometer (Edinburgh Instruments Ltd.) equipped with a closed helium cryostat. The afterglow photographs for $LiTaO_3$:xBi^{2+},yDy^{3+} were taken by an iPhone 12Pro and the X-ray imaging photographs were taken by a Nikon D850 camera. To understand the photochromic phenomenon, reflectivity spectra in the range from 200 to 800 nm were measured by a Shimadzu UV-2550 UV–vis spectrophotometer. For the optically induced coloring and bleaching measurements, a commercial lighting source (WFH-204BS) manufactured by Hangzhou Qiwei Instrument Co., Ltd., China was used, as shown in Figure S26 (Supporting Information). The lights produced by two types of Hg lamps inside the WFH-204BS could be selected by a dark filter to the 254 and 365 nm UV light. The $LiTaO_3$:xBi^{2+},yDy^{3+} phosphor film was horizontally placed under the filter with a distance of 1 cm.

TL glow curves and TL emission (TLEM) spectra were measured. The used setup was equipped with a red-sensitive Hamamatsu R928PPMT, a UV–visible–near infrared spectrometer (Ocean Optics, QE65 Pro), a thermostat, a 50 kV monoblock X-ray tube (TUB00083-2, W target, MOXTEK, Ltd.), a Hg lamp (254 nm UV light), a white-light-emitting diode (WLED), a 365 nm LED, a 396 nm LED, a 656 nm laser, and a 850 nm laser light source. Prior to all thermoluminescence measurements, all compounds were heated to ≈723 K with a duration of ≈4 min to remove captured electrons and holes from traps and then cooled to RT (≈298 K). For TLEM spectra, the TL emission was measured by the QE65 Pro spectrometer. For TL glow curve measurements, the Hamamatsu R928P photomultiplier was used as the detector. A SCHOTT BG-39 filter was placed between the compounds and the R928P photomultiplier. The BG-39 filter has a good transmittance from ≈300 to ≈800 nm. The TL glow curve intensities were corrected for irradiation time and sample mass. X-ray excited emission as a function of time was recorded on the above TL facility. During this measurement, a TUB00083-2 X-ray tube was switched on to generate an X-ray beam to excite a compound, and the integrated emission in the range from 300 to 800 nm was continuously detected by the R928P photomultiplier from 0 to 200 s. For optically stimulated luminescence (OSL) measurements, a compound was first exposed to 254 nm UV light (340 μW cm^{-2}) or X-rays, and then stimulated by different light sources of WLED (52 mW cm^{-2}), 365 nm UV light (384 μW cm^{-2}), 396 nm LED (46 μW cm^{-2}), 656 nm laser (8.5 mW cm^{-2}), or 850 nm laser with different time durations at RT, and finally a thermoluminescence glow curve was measured at a heating rate of 1 K s^{-1}.

To unravel electron and hole trapping and release processes, the TLE curve was measured by using the FLS920 fluorescence spectrometer (Edinburgh Instruments, Ltd.).[27] The $LiTaO_3$:0.005Bi^{3+},0.005Dy^{3+} afterglow phosphor was exposed to different energy photon in the wavelength range from 200 to 400 nm with a duration of 60 s, and then room temperature isothermal decay curves were measured with a duration of 60 s by monitoring the Dy^{3+} characteristic emission at 580 nm. Integrated room temperature isothermal decay intensity from 0 to 60 s was corrected using the wavelength-dependent excitation intensity of the xenon lamp. A so-called TLE curve was constructed in Figure 7b by showing the corrected isothermal Dy^{3+} 580 nm decay intensity as a function of charging wavelength in the range from 200 to 400 nm.

3. Results

3.1. X-Ray Diffraction and Photoluminescence Spectroscopy

High-purity samples are required for the spectroscopy and thermoluminescence study. XRD of the bismuth- and/or dysprosium-doped $LiTaO_3$ were therefore first recorded, and they

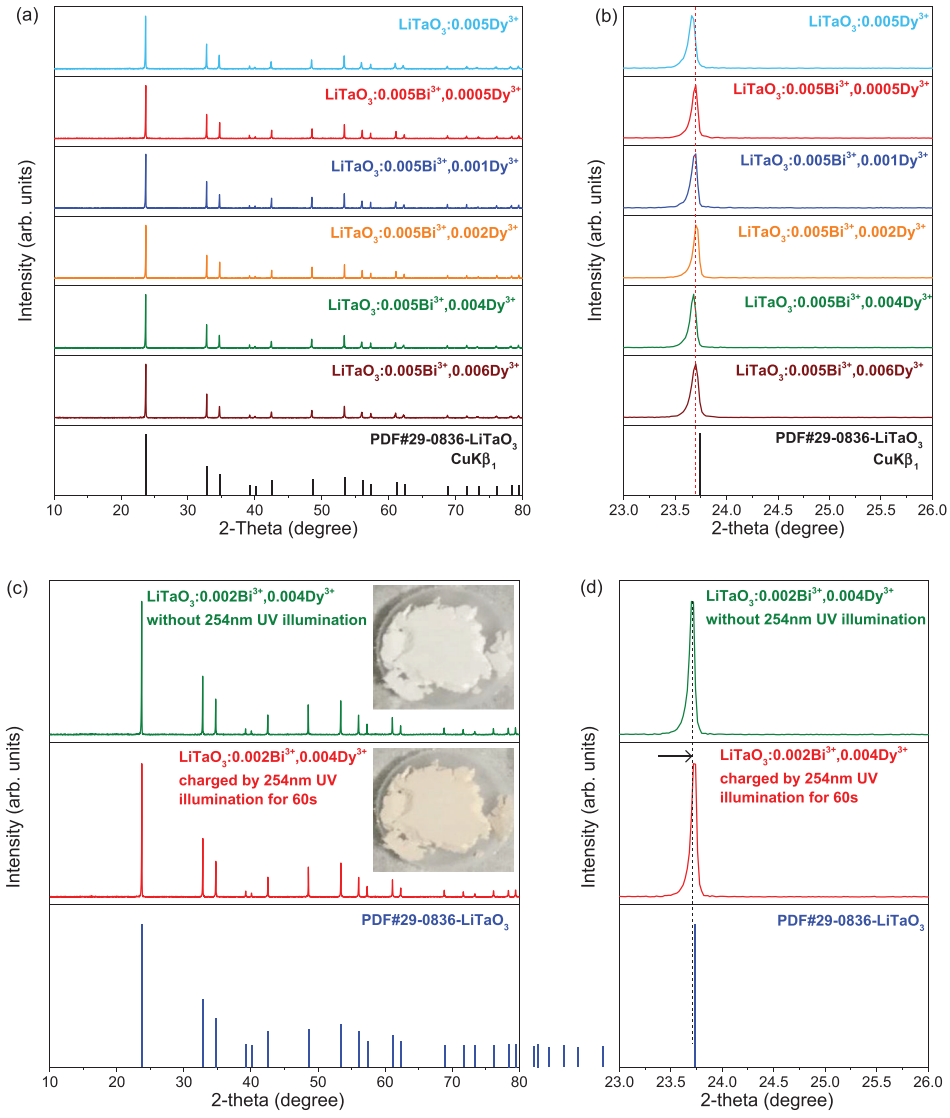

Figure 2. a) XRD patterns from 10° to 80° and b) detailed XRD patterns in the range from 23° to 26° for Bi^{3+} and/or Dy^{3+}vdoped $LiTaO_3$. c) XRD patterns and d) detailed XRD patters for the prepared $LiTaO_3$:0.002Bi^{3+},0.004Dy^{3+} prior to 254 nm UV-light illumination and after 254 nm UV-light illumination. The inset in panel (c) shows the photographs before and after 254 nm UV-light illumination for a duration of 60 s.

are shown in **Figure 2**a,b. All synthesized compounds have a single phase, and their corresponding XRD patterns are consistent with the $LiTaO_3$ reference card (No. PDF#29–0836).

The photochromic phenomenon was observed in $LiTaO_3$:0.002Bi^{3+},0.004Dy^{3+} in the photograph insets of Figure 2c after exposure to 254 nm UV light. To check whether the crystal structure of $LiTaO_3$:0.002Bi^{3+},0.004Dy^{3+} has changed or not after such exposure, its XRD pattern was measured, as shown in Figure 2c. The pattern still matches well with the $LiTaO_3$ reference card (No. PDF#29–0836). Figure 2d further compares the XRD peak near 23.7°, which slightly shifts toward a larger angle after exposure to 254 nm UV light. This indicates that it induces a slight shrinkage of the lattice of $LiTaO_3$:0.002Bi^{3+},0.004Dy^{3+}.

Photographs of the afterglow and photochromic changes of $LiTaO_3$:$x$$Bi^{3+}$,$y$$Dy^{3+}$ have been taken and are shown in **Figure 3** and in Figures S2 and S3 (Supporting Information). Very weak yellow afterglow appears in $LiTaO_3$:0.005Dy^{3+} in Figure 3a3. After co-doping, Bi^{3+} in $LiTaO_3$:0.005Bi^{3+},$y$$Dy^{3+}$, intense afterglow appears and the afterglow color can be tailored from cyan to white by changing the Dy^{3+} concentration, as shown in Figure 3b3,c3. The white afterglow color can further be engineered by changing the Bi^{3+} concentration from 0.005 to 0.002 in $LiTaO_3$:0.002Bi^{3+}, $y$$Dy^{3+}$ as illustrated in Figure S2h3, l3 (Supporting Information). The afterglow spectra and color coordinates for $LiTaO_3$:0.002Bi^{3+},$y$$Dy^{3+}$ (y = 0.0005–0.008) and $LiTaO_3$:0.005Bi^{3+},0.002Dy^{3+} are shown in Figures S7 and S8 (Supporting Information). To further demonstrate the white afterglow in $LiTaO_3$:0.002Bi^{3+},0.004Dy^{3+}, its room-temperature isothermal decay curves and afterglow spectra as a function of time after exposure to 254 nm UV light are shown in Figures S9 and S10 (Supporting Information).

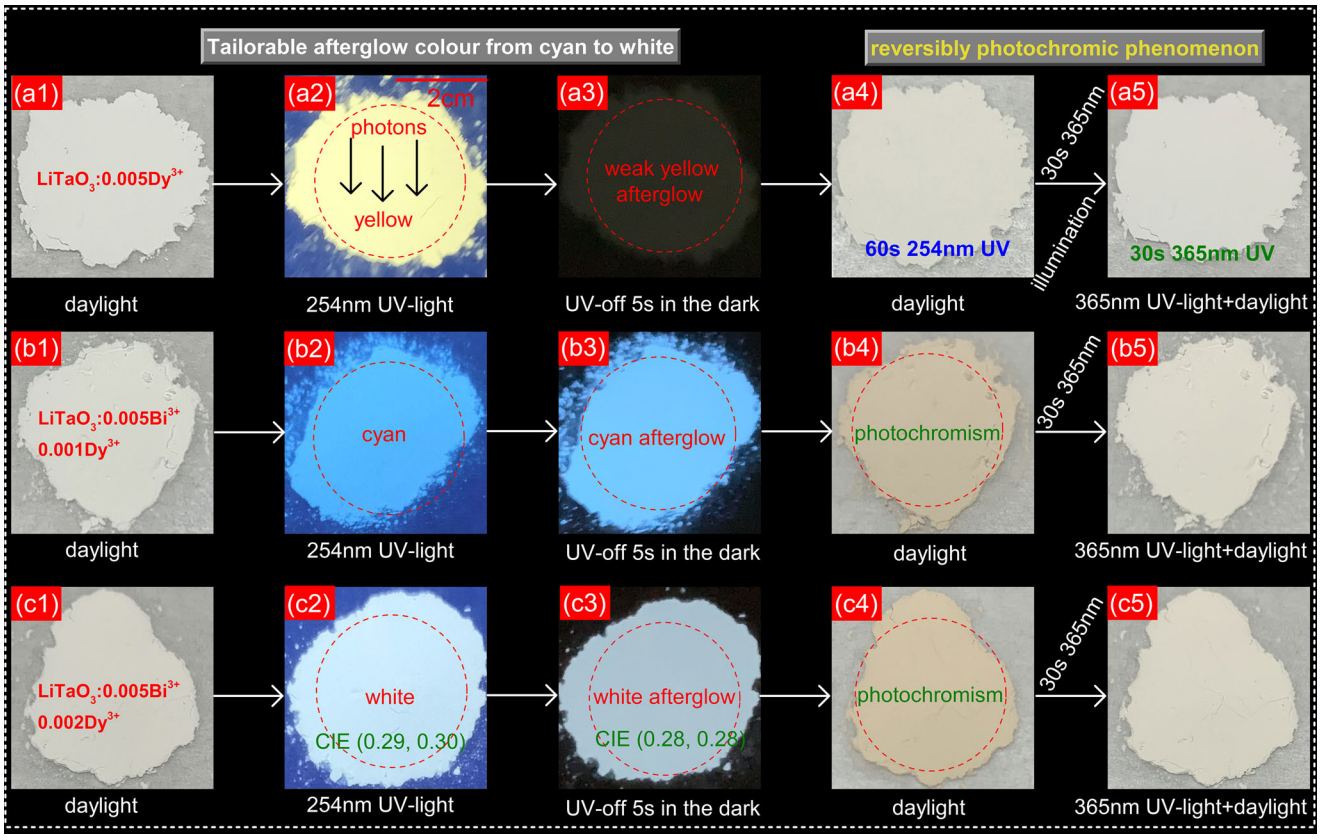

Figure 3. Photographs on rows a), b), and c), pertain to the as-synthesized $LiTaO_3$:0.005Dy^{3+}, $LiTaO_3$:0.005Bi^{3+},0.001Dy^{3+}, and $LiTaO_3$:0.005Bi^{3+},0.002Dy^{3+}, respectively, with column 1) the appearance in daylight, column 2) 254 nm excited photoluminescence, column 3) the afterglow, column 4) photochromic color change, and column 5) the phosphor after bleaching.

Figure 3a–c shows the photographs of $LiTaO_3$:$x$$Bi^{3+}$,$y$$Dy^{3+}$ as synthesized (photos a1, b1, and c1), the photchromic color change after exposure to 254 nm UV light for 60 s (photos a4, b4, and c4), and the reversed color change by 365 nm UV light illumination for 30 s (photos a5, b5, and c5). For $LiTaO_3$:0.005Dy^{3+} in Figure 3a4, a weak photochromic phenomenon appears after 254 nm UV light illumination. After Bi^{3+} co-doping in $LiTaO_3$:0.005Bi^{3+},0.001Dy^{3+}, a much stronger photochromic phenomenon emerges in Figure 3b4. The photochromic contrast increases from $y = 0.0005$ to $y = 0.001$, and then decreases with further increasing y in $LiTaO_3$:0.005Bi^{3+},$x$$Dy^{3+}$, as shown in Figure S3n2–s2 (Supporting Information). The same applies for $LiTaO_3$:0.002Bi^{3+},$y$$Dy^{3+}$ ($y = 0.0005$–0.008) in Figure S3w2–z2 (Supporting Information).

Photoluminescence excitation and emission spectra were recorded and shown in **Figure 4**. Figure 4a shows the excitation spectra of $LiTaO_3$:0.005Bi^{3+},0.005Dy^{3+} recorded at RT by monitoring the Bi^{3+} emission at 435 nm or Dy^{3+} characteristic emission at 580 nm. Typical 4f → 4f excitation bands of Dy^{3+} emerge in the range from 320 to 400 nm. Two broad excitation bands peaked at 252 and 297 nm appear when Dy^{3+} or Bi^{3+} emission was monitored. Photoluminescence excitation (λ_{em} = 583 nm) and emission (λ_{ex} = 300 nm) spectra of $LiTaO_3$:0.005Bi^{3+},0.005Dy^{3+} were also measured at 10 K and are shown in Figure 4b. Two excitation bands peaked near 243 and 300 nm with a shoulder band peaked near 280 nm, and a few sharp line excitation bands between 320 and 500 nm are observed, which will be, respectively, assigned to the intrinsic defect(s), Bi^{3+} excitation A and D bands, and the Dy^{3+} 4f → 4f transitions. The host excitation is at 225 nm from which E_{ex} = 5.5 eV in Figure 1 was obtained. Upon 300 nm excitation, a broad emission band between 350 and 650 nm peaking near 438 nm appears together with narrow bands near 482, 582, and 666 nm, which will be attributed to Bi^{3+} D-band and Dy^{3+} 4f → 4f emissions.

Figure 4c shows the PL spectra of $LiTaO_3$:0.005Bi^{3+},$y$$Dy^{3+}$ upon 300 nm excitation at RT. After Dy^{3+} co-doping, both Bi^{3+} and Dy^{3+} characteristic emissions emerge. With increasing y, the Bi^{3+} emission peaked at 436 nm gradually decreases, which is also illustrated in Figure 4f. To estimate the energy transfer efficiency (η_{ET}) from Bi^{3+} to Dy^{3+} upon 300 nm excitation, we used[28]

$$\eta_{ET} = 1 - \frac{I}{I_0} \quad (1)$$

where I_0 is the Bi^{3+} emission intensity at 436 nm in $LiTaO_3$:0.005Bi^{3+} and I is the Bi^{3+} 436 nm emission intensity in $LiTaO_3$:0.005Bi^{3+},$y$$Dy^{3+}$ (y = 0.005–0.06). The calculated values are given in Figure 4f. Figure 4d shows the PL spectra of $LiTaO_3$:0.005Bi^{3+},$y$$Dy^{3+}$ upon 250 nm excitation. Similar to Figure 4c, with increasing y, the Bi^{3+} emission intensity gradually decreases, while the Dy^{3+} typical 4f → 4f emissions first increase from y = 0.005 to y = 0.02, and then decrease from y = 0.02 to y = 0.06. Figure 4e and Figure S5 (Supporting Infor-

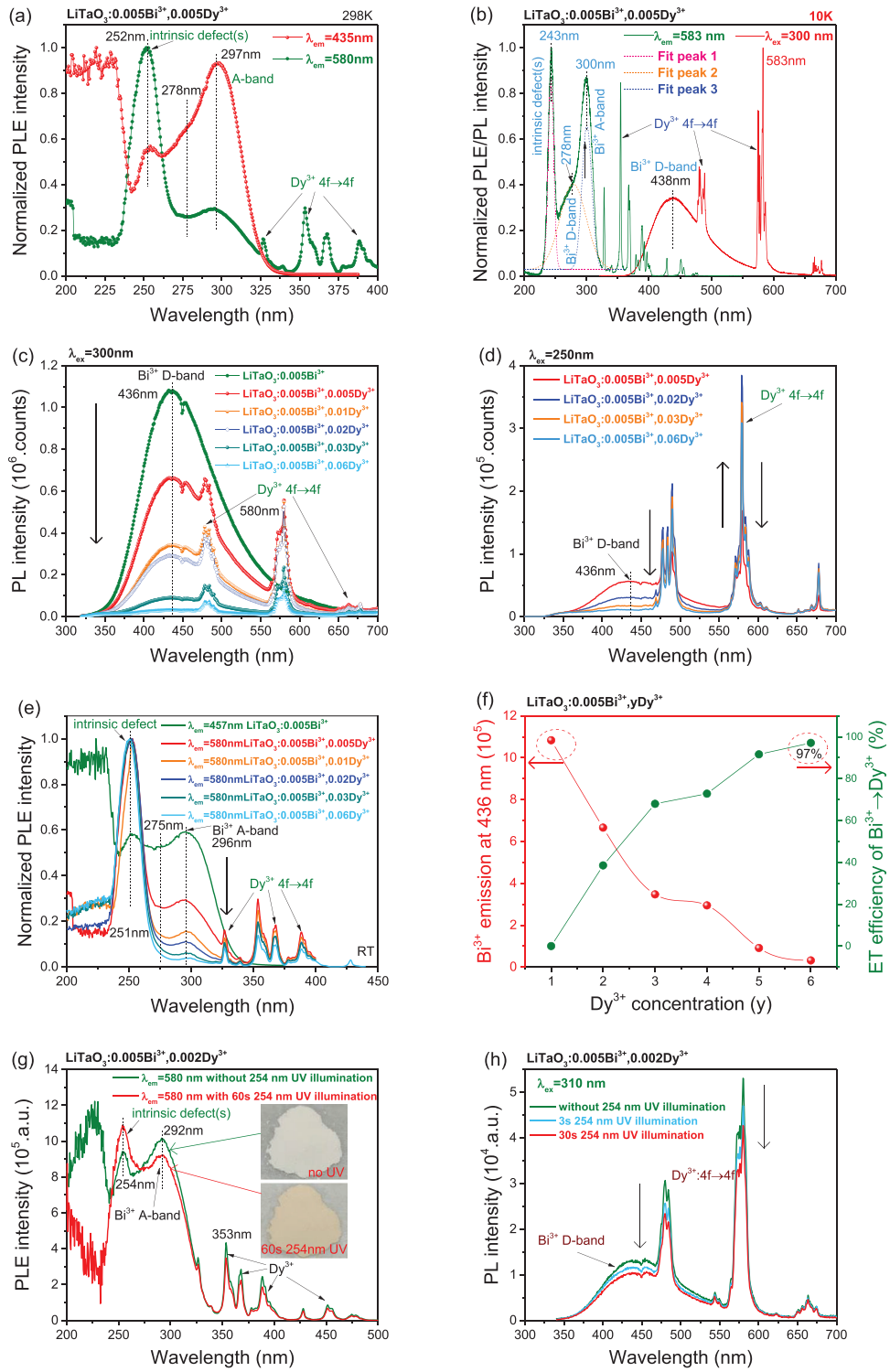

Figure 4. Photoluminescence excitation (PLE) and emission (PL) spectra for $LiTaO_3$:0.005Bi^{3+}, 0.005Dy^{3+} measured at a) RT and b) 10 K, and c) until e) $LiTaO_3$:0.005Bi^{3+},yDy^{3+} ($y = 0$ until 0.06) measured at RT. f) Bi^{3+} emission intensity at 436 nm and the calculated energy transfer efficiency (ET) from Bi^{3+} to Dy^{3+} in $LiTaO_3$:0.005Bi^{3+},yDy^{3+} ($y = 0$ until 0.06). g) and h) PLE ($\lambda_{em} = 580$ nm) and PL ($\lambda_{ex} = 310$ nm) spectra for $LiTaO_3$:0.005Bi^{3+},0.002Dy^{3+} after exposure to 254 nm UV light. The inset in panel (g) shows the color change after exposure to 254 nm UV light.

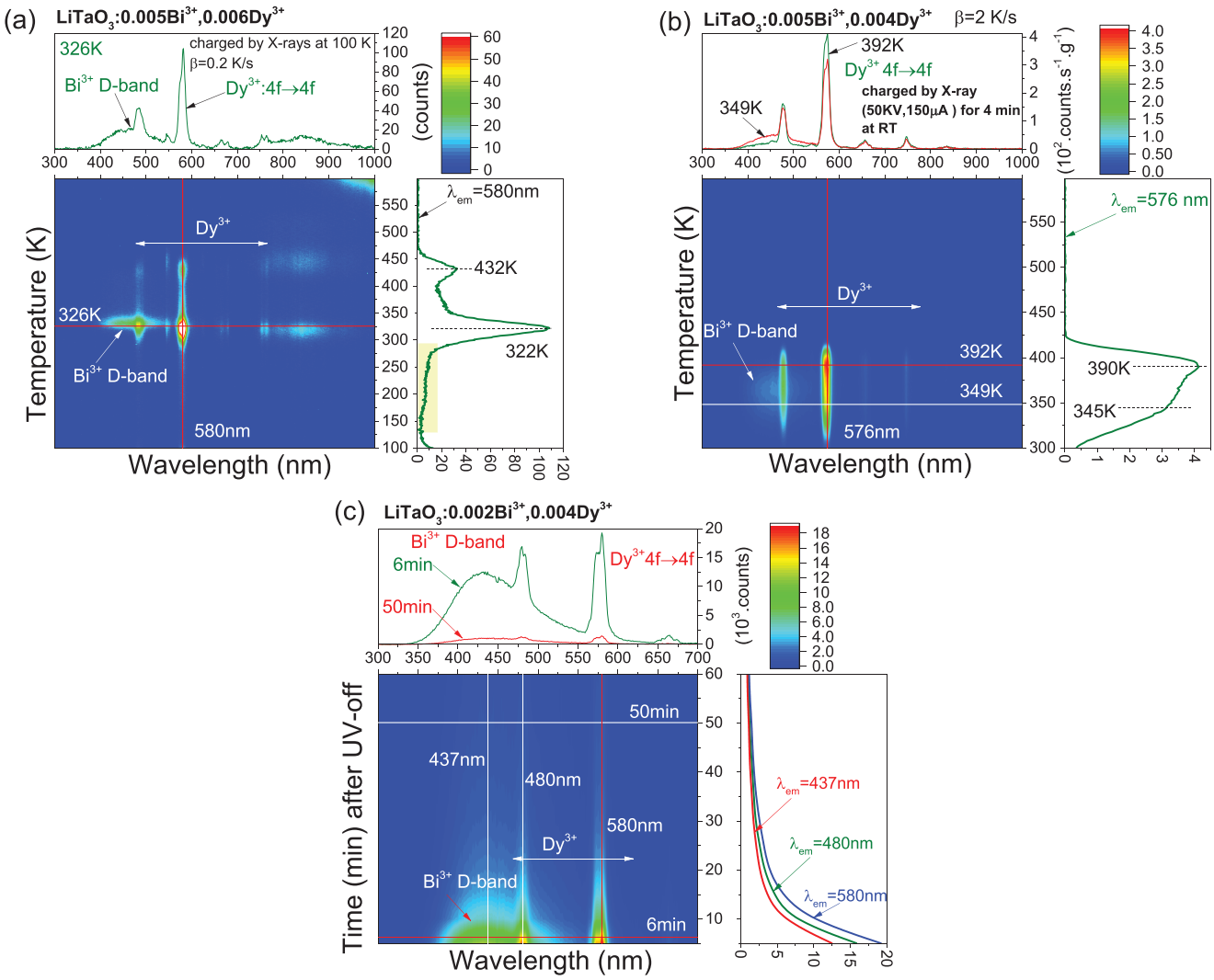

Figure 5. a) The above 100 K TLEM plot measured at $\beta = 0.2$ K s^{-1} for $LiTaO_3$:0.005Bi^{3+}, 0.006Dy^{3+} after exposure to X-rays at 100 K, b) above-RT TLEM plot measured at $\beta = 2$ K s^{-1} for $LiTaO_3$:0.005Bi^{3+},0.004Dy^{3+} after exposure to X-rays at ≈298 K. c) RT (≈298 K) isothermal decay spectra for $LiTaO_3$:0.002Bi^{3+},0.004Dy^{3+} as a function of time after exposure to 254 nm UV light in the dark.

mation) show the normalized at 250 nm and unnormalized excitation spectra for $LiTaO_3$:0.005Bi^{3+},$y$$Dy^{3+}$. With increasing y, the excitation band near 296 nm gradually decreases, while the excitation band near 250 nm first gradually increases from y = 0.005 to y = 0.02, and then decreases from y = 0.02 to y = 0.06 in $LiTaO_3$:0.005Bi^{3+},$y$$Dy^{3+}$. Figure S6 (Supporting Information) shows the PLE (λ_{em} = 580 nm) and PL (λ_{ex} = 298 nm) spectra of $LiTaO_3$:0.002Bi^{3+},$y$$Dy^{3+}$.

To understand the photochromic phenomenon, the photoluminescence excitation and emission spectra of $LiTaO_3$:0.005Bi^{3+},0.002Dy^{3+} were recorded after exposure to 254 nm UV light and shown in Figure 4g,h. The excitation band near 254 nm increases, while the excitation band near 292 nm and the Dy^{3+} 4f → 4f excitation bands decrease after 254 nm UV-light illumination in Figure 4g. Figure 4h shows that both the Bi^{3+} emission band near 440 nm and Dy^{3+} 4f→4f emission lines gradually decrease as a function of 254 nm UV-light illumination time.

3.2. Unraveling Charge-Carrier Trapping Processes by Thermoluminescence

To unravel the persistent luminescence found in Figure 3b3,c3 and to identify the recombination centers in bismuth- and dysprosium-doped $LiTaO_3$, TLEM spectra were measured. **Figure 5**a shows the >100 K TLEM plot for $LiTaO_3$:0.005Bi^{3+},0.006Dy^{3+} recorded at a heating rate of 0.2 K s^{-1} after exposure to X-rays at 100 K. Both characteristic Bi^{3+} and Dy^{3+} emissions with a TL peak near 432 K and a TL peak near 322 K with a shoulder extending from 300 to 150 K appear. Figure 5b shows an above-RT TLEM plot for $LiTaO_3$:0.005Bi^{3+},0.004Dy^{3+} measured at a heating rate of 2 K s^{-1} after exposure to X-rays at 298 K. Two TL glow peaks near 345 and 390 K with Bi^{3+} and Dy^{3+} typical emissions were observed. Afterglow is expected when TL glow peaks near RT are observed as in Figure 5a,b. Afterglow spectra as a function of time for $LiTaO_3$:0.002Bi^{3+},0.004Dy^{3+} after 254 nm UV-light charging

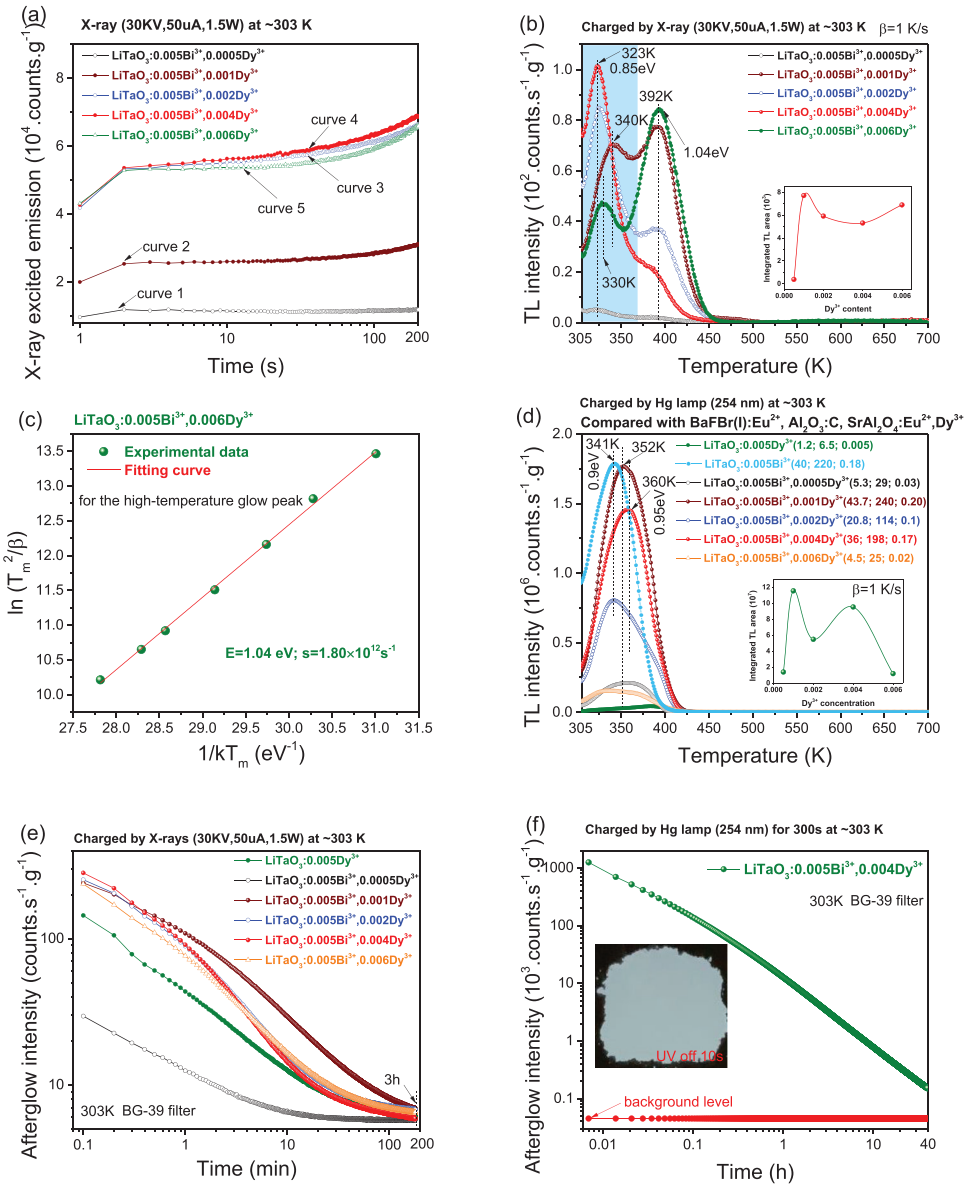

Figure 6. a) X-ray excited Bi^{3+} and Dy^{3+} integrated emission intensity from 300 to 800 nm as a function of time, TL glow curves at $\beta = 1$ K s^{-1} for $LiTaO_3$:0.005Bi^{3+},yDy^{3+} after exposure to b) X-rays and d) 254 nm UV light. c) A variable heating rate plot of $LiTaO_3$:0.005Bi^{3+}, 0.006Dy^{3+} after exposure to X-rays. Isothermal decay curves for e) $LiTaO_3$:0.005Bi^{3+},yDy^{3+} after exposure to X-rays and for f) $LiTaO_3$:0.005Bi^{3+},0.004Dy^{3+} after exposure to 254 nm UV light at ≈303 K. The Bi^{3+} and Dy^{3+} emissions were monitored. The inset in panel (f) shows an afterglow photograph after stopping the 254 nm UV-light excitation. The insets in panels (b) and d) are the integrated TL intensities from 305 to 700 K as a function of Dy^{3+} concentration in $LiTaO_3$:0.005Bi^{3+},yDy^{3+}. The ratios from left to right in the legend in panel (d), respectively, compare the integrated TL intensities from 305 to 700 K of $LiTaO_3$:0.005Bi^{3+},yDy^{3+} to that of commercial BaFBr(I):Eu^{2+}, Al_2O_3:C, or $SrAl_2O_4$:Eu^{2+},Dy^{3+} recorded under the same conditions.

were recorded and shown in Figure 5c. Both the Bi^{3+} and Dy^{3+} afterglow spectra are measurable more than 1 h.

Upon X-ray exposure, created free charge carriers can either be trapped or recombined to generate luminescence. With time the traps are being filled and more charge carriers are available for luminescence. These processes can be studied by recording the X-ray excited emission intensity as a function of time combined with the TL glow curves. We studied the $LiTaO_3$:0.005Bi^{3+},yDy^{3+} compounds as a function of Dy^{3+} concentration in **Figure 6**a,b. We did the same for $LiTaO_3$:0.002Bi^{3+},yDy^{3+} with a lower Bi^{3+} concentration in Figures S11 and S12 (Supporting Information). Figure 6a shows the X-ray excited emission intensity as a function of time for $LiTaO_3$:0.005Bi^{3+},yDy^{3+}. In this measurement, a compound was exposed to an X-ray beam, and the integrated intensity of the X-ray excited Bi^{3+} and Dy^{3+} emissions from 300 to 800 nm was recorded by a photomultiplier with a SCHOTT BG-39 filter. Curve (1) with 0.0005Dy^{3+} has the lowest integrated intensity from 0 to 200 s. The integrated intensity increases with increasing Dy^{3+} concentration (y) to become maximum for $y = 0.004$ (curve 4) and then decreases again for $y = 0.006$ (curve

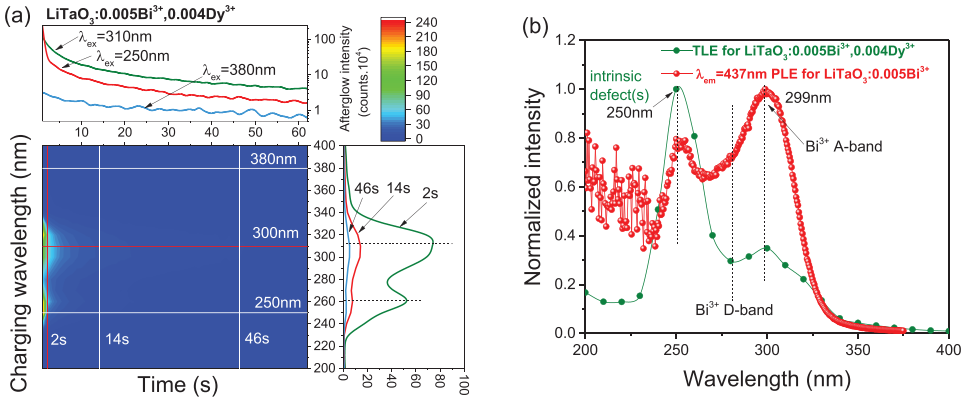

Figure 7. a) 2D contour plot for room temperature (298 K) isothermal decay curves for $LiTaO_3$:0.005Bi^{3+},0.004Dy^{3+} as a function of charging wavelength in the range from 200 to 400 nm. The Dy^{3+} emission at 580 nm was monitored during this measurement. b) A comparison of the photoluminescence excitation spectrum of $LiTaO_3$:0.005Bi^{3+} (λ_{em} = 437 nm) and the thermoluminescence excitation (TLE) curves of $LiTaO_3$:0.005Bi^{3+},0.004Dy^{3+}.

5). TL glow curves of $LiTaO_3$:$x$$Bi^{3+}$,$y$$Dy^{3+}$ have been studied after exposure to X-rays or 254 nm UV light. Figure 6b shows the TL glow curves of $LiTaO_3$:0.005Bi^{3+},$y$$Dy^{3+}$ after exposure to X-rays at 303 K. TL glow peaks near 323 and 392 K were observed, which will be assigned to electron liberation from host intrinsic defects. Similar TL glow peaks near 326 and 387 K also emerge in X-ray charged $LiTaO_3$:0.002Bi^{3+}, $y$$Dy^{3+}$ in Figure S12 (Supporting Information). Because $LiTaO_3$:0.005Bi^{3+},0.006Dy^{3+} shares the common TL glow peaks near ≈323 and ≈392 K that are also observed for the other compounds, we studied the $LiTaO_3$:0.005Bi^{3+},0.006Dy^{3+} compound in more detail to analyze these TL glow peaks as shown in Figure S14 (Supporting Information). The trapping depth (E) of $LiTaO_3$:0.005Bi^{3+},0.006Dy^{3+} can be determined by a variable heating rate plot and the following equation[16,29]

$$\ln\left(\frac{T_m^2}{\beta}\right) = \frac{E}{kT_m} + \ln\left(\frac{E}{ks}\right) \quad (2)$$

in which s means the frequency factor, T_m denotes the TL glow peak maximum, k denotes the Boltzmann constant (8.62 × 10^{-5} eV K^{-1}), and β means the utilized heating rate from 0.2 to 6.4 K s^{-1} as demonstrated in Figure S14 (Supporting Information). Figure 6c shows the variable heating rate plot for $LiTaO_3$:0.005Bi^{3+},0.006Dy^{3+}, which derives a frequency factor of 1.80 × 10^{12} s^{-1} and a trap depth of 1.04 eV for the 392 K TL peak. The trapping depth for the 323 K TL peak is calculated to be ≈0.85 eV based on Equation (2) with the obtained frequency factor of 1.80 × 10^{12} s^{-1}, β = 1 K s^{-1}, and T_m = 323 K.

Figure 6d shows the TL glow curves of Bi^{3+}- and/or Dy^{3+}-doped $LiTaO_3$ after exposure to 254 nm UV light at 303 K. Very weak TL glow is observed in $LiTaO_3$:0.005Dy^{3+}. Intense and broad TL glow peaks near ≈341–360 K in the range from 305 to 425 K appear in $LiTaO_3$:0.005Bi^{3+},$y$$Dy^{3+}$. The ratios of integrated TL intensities from 303 to 700 K of $LiTaO_3$:0.005Bi^{3+},$y$$Dy^{3+}$ to that of the commercial BaFBr(I):Eu^{2+}, Al_2O_3:C chip, and $SrAl_2O_4$:Eu^{2+},Dy^{3+} are given in the legend of Figure 6d. $LiTaO_3$:0.005Bi^{3+},0.001Dy^{3+} has the strongest integrated TL intensity, which is about 44, 240, and 0.2 times higher than that of the commercial BaFBr(I):Eu^{2+}, Al_2O_3:C chip, and $SrAl_2O_4$:Eu^{2+},Dy^{3+} after 254 nm UV-light charging. There is an obvious difference in the TL glow curves of $LiTaO_3$:0.005Bi^{3+}, 0.001Dy^{3+} recorded after exposure to X-rays in Figure 6b and 254 nm UV light in Figure 6d. Possibly there is a trap depth distribution in $LiTaO_3$:0.005Bi^{3+},0.001Dy^{3+} and the traps can be filled differently during X-rays or 254 nm UV-light illumination. To testify the trap distribution, a peak cleaning method has been used for $LiTaO_3$:0.005Bi^{3+},0.001Dy^{3+}.[30] Figure S15a (Supporting Information) shows that the TL glow peak (T_m) near 349 K shifts toward a higher temperature and the TL intensity continuously decreases with the increase of the peak clean temperature (T_{clean}). It means that a trap depth distribution exists in $LiTaO_3$:0.005Bi^{3+},0.001Dy^{3+}, which ranges from about ≈0.69 to ≈0.71 eV as determined from Figure S15b (Supporting Information). The T_m shift toward a higher temperature is because electrons trapped in less deep traps have been liberated at T_{clean} and only the electrons captured at deeper traps in $LiTaO_3$:0.005Bi^{3+}, 0.001Dy^{3+} remain.

To evaluate afterglow properties, isothermal decay curves at ≈303 K for $LiTaO_3$:0.005Bi^{3+},$y$$Dy^{3+}$ were measured and shown in Figure 6e,f. Figure 6e shows that more than 3 h Bi^{3+} and Dy^{3+} white afterglow is recordable in $LiTaO_3$:0.005Bi^{3+},$y$$Dy^{3+}$ at ≈303 K and $LiTaO_3$:0.005Bi^{3+},0.004Dy^{3+} has the strongest initial (≈20 s) white afterglow intensity after X-ray charging. Figure 6f further demonstrates that more than 40 h white afterglow is measurable in $LiTaO_3$:0.005Bi^{3+},0.004Dy^{3+} after 254 nm UV-light charging at ≈303 K.

Figure 7a shows the 2D contour plot of RT isothermal decay curves of $LiTaO_3$:0.005Bi^{3+}, 0.004Dy^{3+} after exposure to different energy photons from 200 to 400 nm with a duration of 60 s. Figure 7b compares the TLE plot of $LiTaO_3$:0.005Bi^{3+},0.004Dy^{3+} with the PLE spectrum of $LiTaO_3$:0.005Bi^{3+} at RT. The traps in $LiTaO_3$:0.005Bi^{3+},0.004Dy^{3+} can be filled by the intrinsic defect(s) excitation band peaked near 250 nm, and the Bi^{3+} excitation A-band and D-band.

3.3. Photochromic Phenomenon in $LiTaO_3$:$x$$Bi^{3+}$,$y$$Dy^{3+}$

Figure 3 demonstrated the photochromic color change of the Bi^{3+} and Dy^{3+} co-doped $LiTaO_3$ samples which we further studied by recording reflectivity spectra. **Figure 8**a shows the reflectivity spectra of $LiTaO_3$:0.005Bi^{3+},0.004Dy^{3+} as a function of

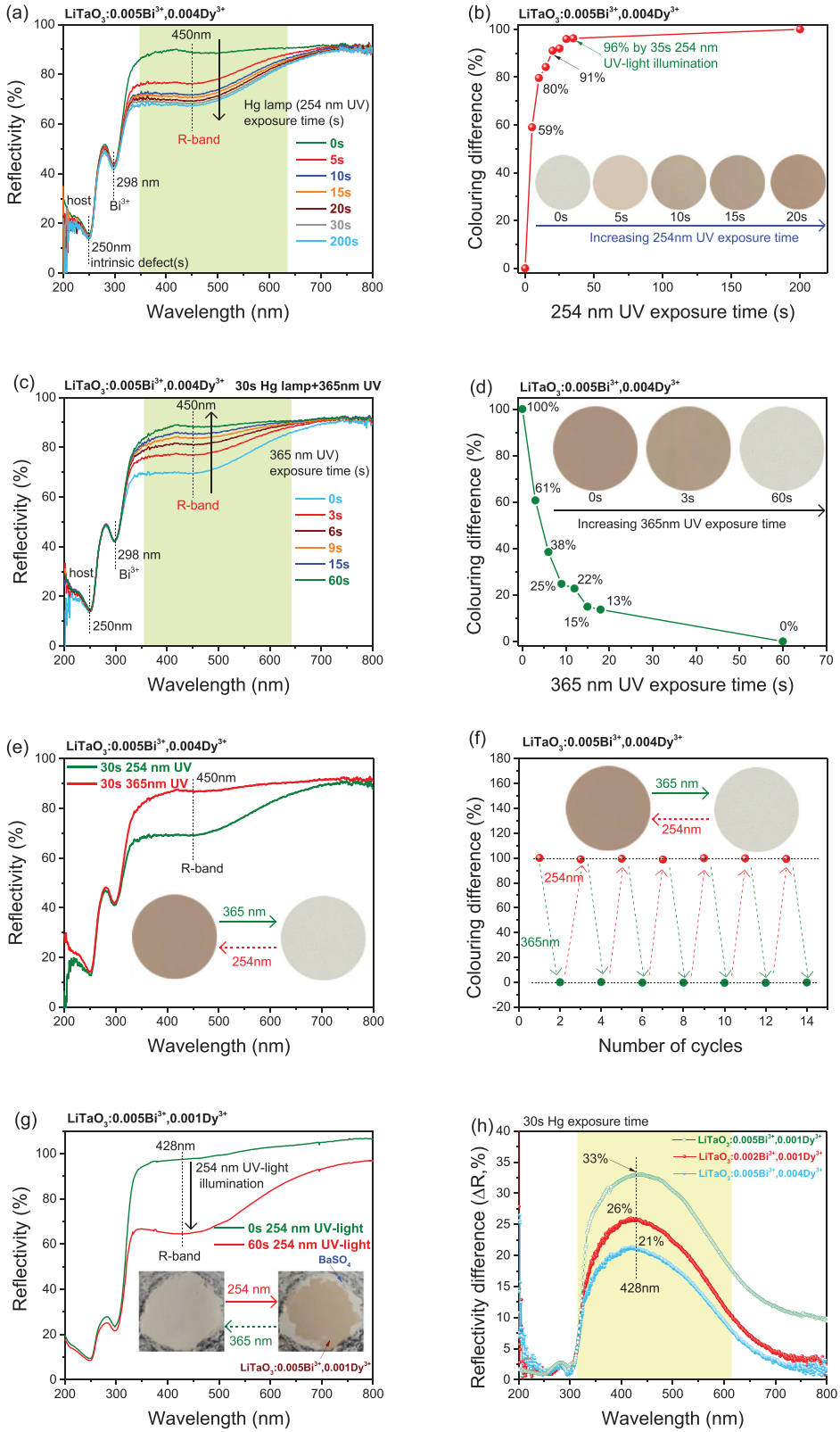

Figure 8. Reflectivity spectra and coloring difference for $LiTaO_3$:0.005Bi^{3+},0.004Dy^{3+} as a function of exposure time of a) and b) 254 nm UV light and c) and d) 365 nm UV light. e) and f) Stability test of the reflectivity spectra and corresponding coloring difference with 254 and 365 nm UV-light illumination for $LiTaO_3$:0.005Bi^{3+},0.004Dy^{3+}. g) and h) Reflectivity spectra and reflectivity difference for the optimized $LiTaO_3$:xBi^{3+},yDy^{3+} (x = 0.002 or 0.005; y = 0.001 or 0.004).

254 nm UV-light illumination time. The host intrinsic defect(s) and Bi-related absorption bands near 250 and 298 nm remain unchanged, while the intensity of a newly observed broad absorption band from 315 to 750 nm, hereafter named the R-band, continuously increases with increasing illumination time from 0 to 200 s. The absolute reflectivity difference at 450 nm before and after 254 nm illumination with 0–200 s duration time increases from 0% for $t = 0$ s to ≈22% for $t = 200$ s. In Figure 8b, the coloring difference is defined as 100% when the absolute reflectivity difference at 450 nm is largest (≈22%). The same applies to Figure 8c,d where the coloring difference is defined as 100% when the 254 nm illumination time is 30 s. Figure 8b shows the coloring difference for $LiTaO_3$:0.005Bi^{3+},0.004Dy^{3+} as a function of 254 nm illumination time. After 5 or 10 s 254 nm illumination, the coloring difference has increased to ≈60% or ≈80% of its maximum value. This indicates that the 254 nm UV-light-induced photochromic process in $LiTaO_3$:0.005Bi^{3+},0.004Dy^{3+} compound is rapid as also illustrated by the photographs in the inset of Figure 8b when a commercial Hg lamp (WFH-204BS) is used.

Figure 8c,d shows the reflectivity spectra and coloring difference for $LiTaO_3$:0.005Bi^{3+},0.004Dy^{3+} after first exposure during 30 s to 254 nm UV light to achieve photochromic coloring, which is then followed by 365 nm UV-light illumination to reverse the coloring. With increasing 365 nm illumination time from 0 to 60 s, the absorption intensity of the *R*-band between 315 and 750 nm gradually decreases in Figure 8c, while the coloring difference monotonously decreases from 100% to 0% in Figure 8d. It means that there is a rapid and reversible photochromic process in $LiTaO_3$:0.005Bi^{3+},0.004Dy^{3+}, as evidenced in Figure 8d.

For information storage application, the reversibility of the photochromic process is important. Figure 8e shows the reflectivity spectra for $LiTaO_3$:0.005Bi^{3+},0.004Dy^{3+} after exposure to 254 nm UV light for 30 s and then followed by 365 nm UV light for 30 s. The above exposure sequence has been repeated six times. Figure 8f shows the coloring difference as a function of the number of cycles. It implies that the 254 or 365 nm UV-light-induced photochromic processes in $LiTaO_3$:0.005Bi^{3+},0.004Dy^{3+} are reversible and also very stable.

To optimize the photochromic phenomenon in Bi^{3+} and Dy^{3+} co-doped $LiTaO_3$, we synthesized $LiTaO_3$:*x*Bi^{3+},*y*Dy^{3+} samples with changing Bi^{3+} or Dy^{3+} concentration as in Figure 3 and in Figure S3 (Supporting Information), and also adjusted the synthesis temperature as in Figures S18–S22 (Supporting Information). Figure 8g shows the reflectivity spectra of the optimized $LiTaO_3$:0.005Bi^{3+},0.001Dy^{3+} after 0 and 60 s 254 nm UV-light illumination. Figure 8h compares the reflectivity difference for the optimized $LiTaO_3$:0.005Bi^{3+},0.004Dy^{3+}, $LiTaO_3$:0.002Bi^{3+},0.001Dy^{3+}, and $LiTaO_3$:0.005Bi^{3+},0.001Dy^{3+} after 254 nm UV-light illumination for 30 s at RT. $LiTaO_3$:0.005Bi^{3+},0.001Dy^{3+} has the largest absorption difference value of ≈33% at 428 nm in Figure 8h and also has the strongest integrated TL intensity as shown in Figure 6d.

For the development of smart light-sensing materials, the TL properties of $LiTaO_3$:*x*Bi^{3+},*y*Dy^{3+} after exposure to 254 nm UV light or X-rays with various doses, and different energy photon stimulations were studied. **Figure 9**a shows the TL glow curves for $LiTaO_3$:0.005Bi^{3+},0.004Dy^{3+} charged by 254 nm UV-light exposure with a duration of 5–35 s. The inset in Figure 9a shows that the integrated TL intensity from 305 to 600 K linearly increases with increasing time from 0 to 30 s. It implies that $LiTaO_3$:0.005Bi^{3+},0.004Dy^{3+} can be used as a potential dosimeter for 254 nm UV-light detection. $LiTaO_3$:0.002Bi^{3+},0.004Dy^{3+} was put into water for a duration of 2.5 h and then dried at 70 °C for 0.5 h before TL measurement. TL glow curves after charging by X-rays are shown in Figure S23 (Supporting Information). TL intensity is still 88% of its initial TL intensity with no exposure to water. It also shows good photochromic phenomenon and intense white afterglow as verified by the photographs in the inset of Figure S23 (Supporting Information).

To study the optically stimulated de-charging, Figure 9b shows the TL glow curves of $LiTaO_3$:0.005Bi^{3+},0.001Dy^{3+} after exposure to 254 nm UV light and then followed by different energy photon stimulation. The TL intensity decreases and the TL peak shifts toward a higher temperature with 850, 656, 396, and 365 nm, and WLED stimulation with a duration time of 10 s. It indicates that the charge carriers captured at less deep traps are removed by low-energy and long-wavelength optical stimulation. Compared with the RT isothermal decay curve after exposure to 254 nm UV light in Figure 9e4, a stronger Bi^{3+} and Dy^{3+} afterglow intensity appears from 60 to 180 s in Figure 9e3 when the phosphor is stimulated by the 850 nm laser beam. An increased afterglow intensity after X-ray charging emerges also in Figure 9e1 when the 850 nm laser beam is switched on from 60 to 180 s. These results suggest that 850 nm optical stimulation removes the charge carriers from the traps in $LiTaO_3$:0.005Bi^{3+},0.004Dy^{3+} and that leads to recombination luminescence at Bi^{3+} and Dy^{3+}. Figure 9c,d further demonstrates that the stored charge carriers in $LiTaO_3$:0.005Bi^{3+},0.001Dy^{3+} can be efficiently removed by WLED for 3 s or 365 nm UV-light stimulation for 15 s. Particularly, the photographs in Figure 9c suggests that when the photochromic $LiTaO_3$:0.005Bi^{3+},0.001Dy^{3+} is bleached by WLED stimulation, the corresponding TL intensity decreased to zero. Upon 656 nm red laser stimulation in Figure 9f3, the charge carriers in less deep traps in the $LiTaO_3$:0.005Bi^{3+},0.004Dy^{3+}-based phosphor area have been removed, which then gives less Bi^{3+}- and Dy^{3+}-based white afterglow. This feature has been utilized to show the text information of "1, 2, and 3" in the $LiTaO_3$:0.005Bi^{3+}, 0.004Dy^{3+}-based film in the dark as in Figure 9g1–g3.

3.4. Exploring a Smart Optical-Sensing Phosphor for Information Storage and X-Ray Imaging

The developed $LiTaO_3$:*x*Bi^{3+},*y*Dy^{3+} phosphors have been explored as optical-sensing materials for 2D image information storage or X-ray imaging applications. **Figure 10**a shows how to make a flexible film based on a phosphor and silica gel. Figure S24a1 (Supporting Information) shows such a $LiTaO_3$:0.005Bi^{3+},0.002Dy^{3+}-based film (film 1). Figure 10b shows how to realize information storage by using the synthesized films. Figure 10c first shows that information can be stored by an X-ray-induced photochromic phenomenon. Figure 10d1,d2 shows that the text of "WX" can be stored in the $LiTaO_3$:0.005Bi^{3+},0.002Dy^{3+}-based film by a 254 nm UV-light-induced photochromic phenomenon. The text of "WX" is visible in the dark because of the Bi^{3+} and Dy^{3+} afterglow from

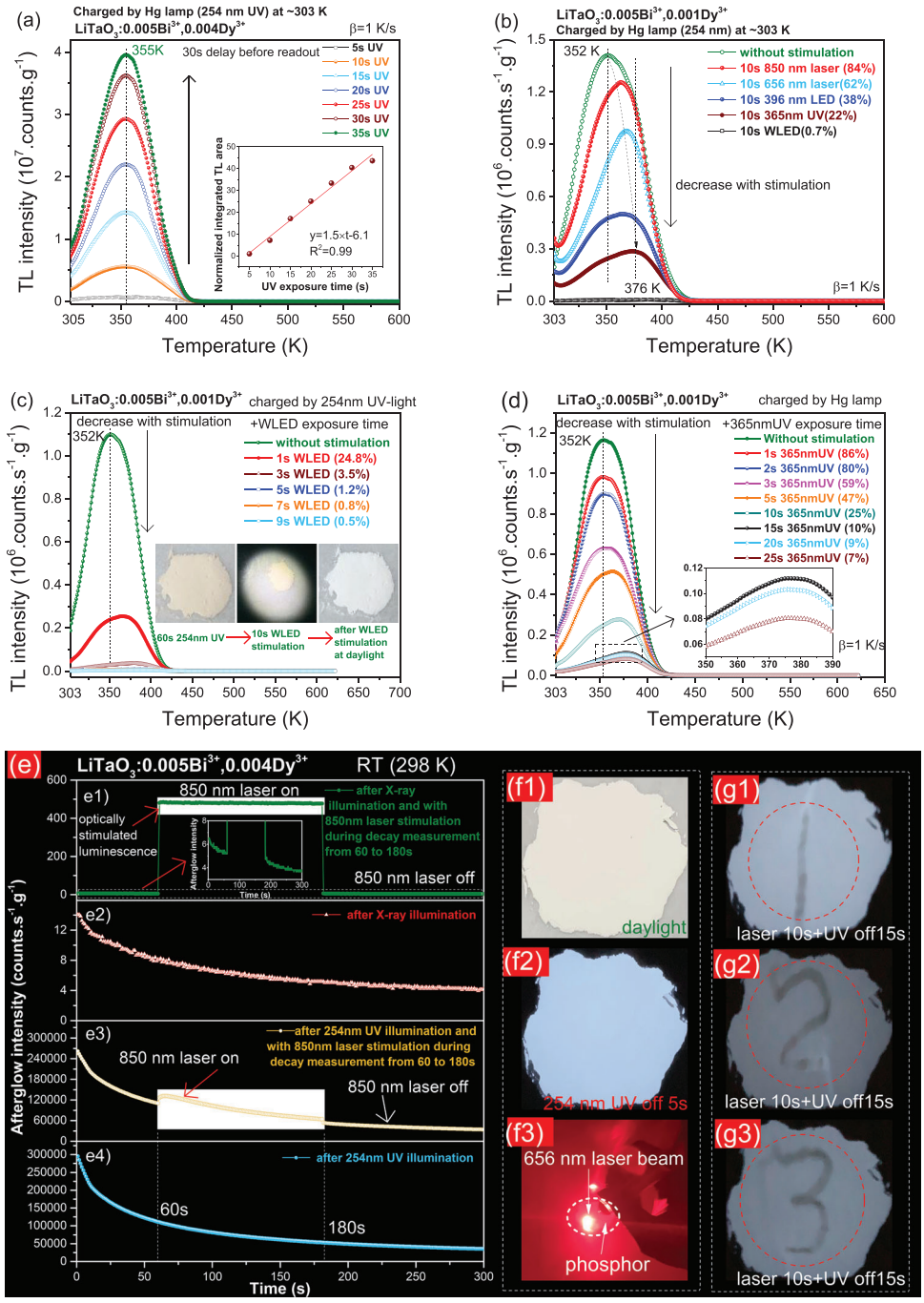

Figure 9. a) TL glow curves at $\beta = 1$ K s^{-1} of $LiTaO_3$:0.005Bi^{3+},0.004Dy^{3+} after exposure to 254 nm UV light with different duration time. TL glow curves measured at $\beta = 1$ K s^{-1} for $LiTaO_3$:0.005Bi^{3+}, 0.001Dy^{3+} after exposure to 254 nm UV-light followed by b) different energy photon stimulation, or with c) WLED and d) 365 nm UV-light stimulation with different duration times. e) RT isothermal decay curves of $LiTaO_3$:0.005Bi^{3+},0.004Dy^{3+} after exposure to X-rays or 254 nm UV light followed by 850 nm laser stimulation for 120 s from 60 to 180 s. The inset in panel (e1) is the enlarged decay curve. f) and g) Information display of "1, 2, and 3" by utilizing the afterglow and the optically stimulated emission phenomenon in $LiTaO_3$:0.005Bi^{3+},0.004Dy^{3+}. The inset in panel (a) shows the integrated TL intensity as a function of 254 nm exposure time and the inset in panel (c) shows the color change after WLED stimulation.

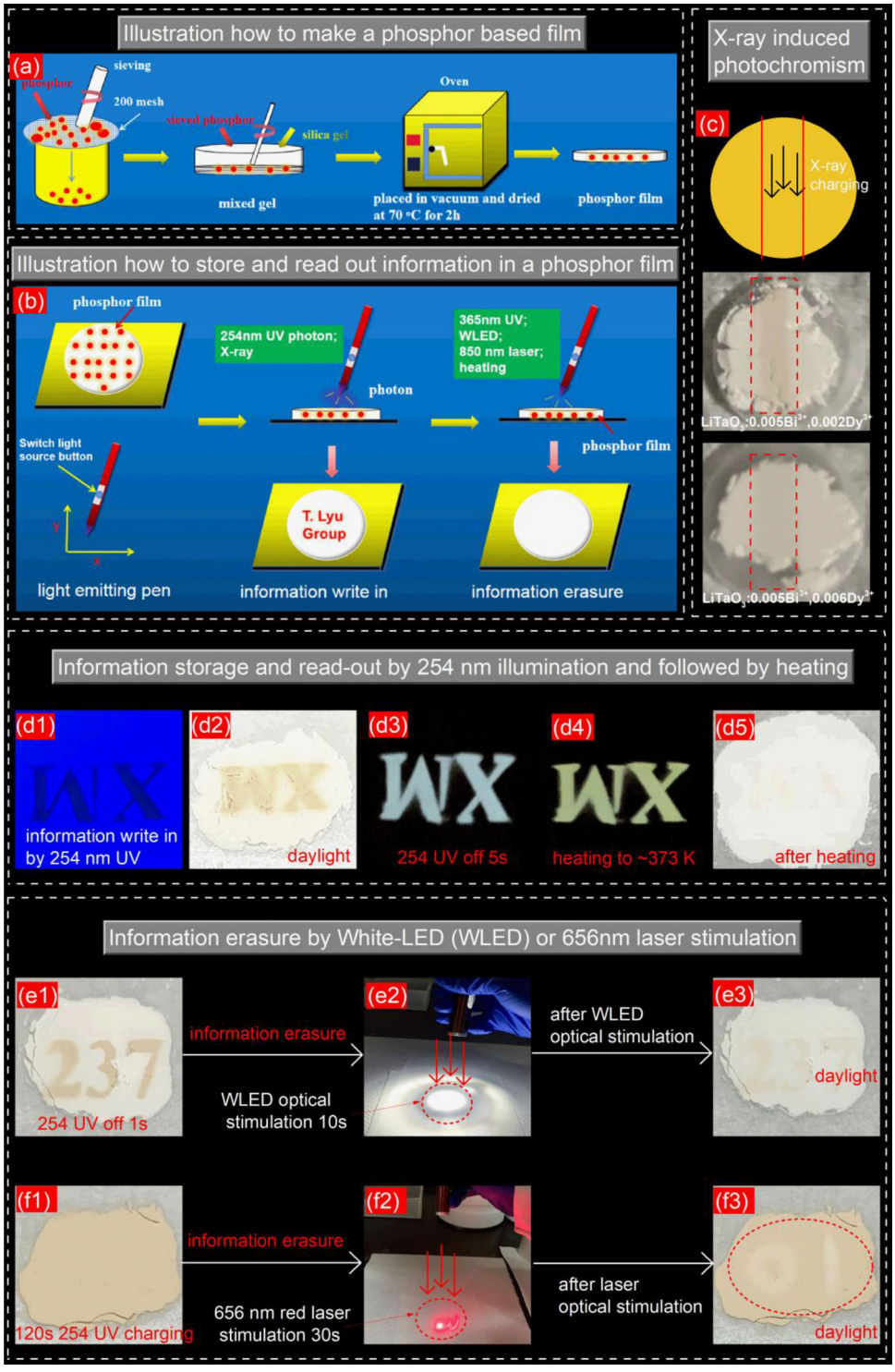

Figure 10. a) Demonstration how to make an optical film by using phosphor dispersed in silicone gel. b) Illustration of information write in and erasure by light stimulation in phosphor film. c) X-rays induced color change for $LiTaO_3$:0.005Bi^{3+},0.002Dy^{3+} and $LiTaO_3$:0.005Bi^{3+},0.006Dy^{3+}. d) until f) Text information write in and erasure of "WX," "237," and "01" in $LiTaO_3$:0.005Bi^{3+},0.002Dy^{3+} by different light stimulation and thermal bleaching treatment.

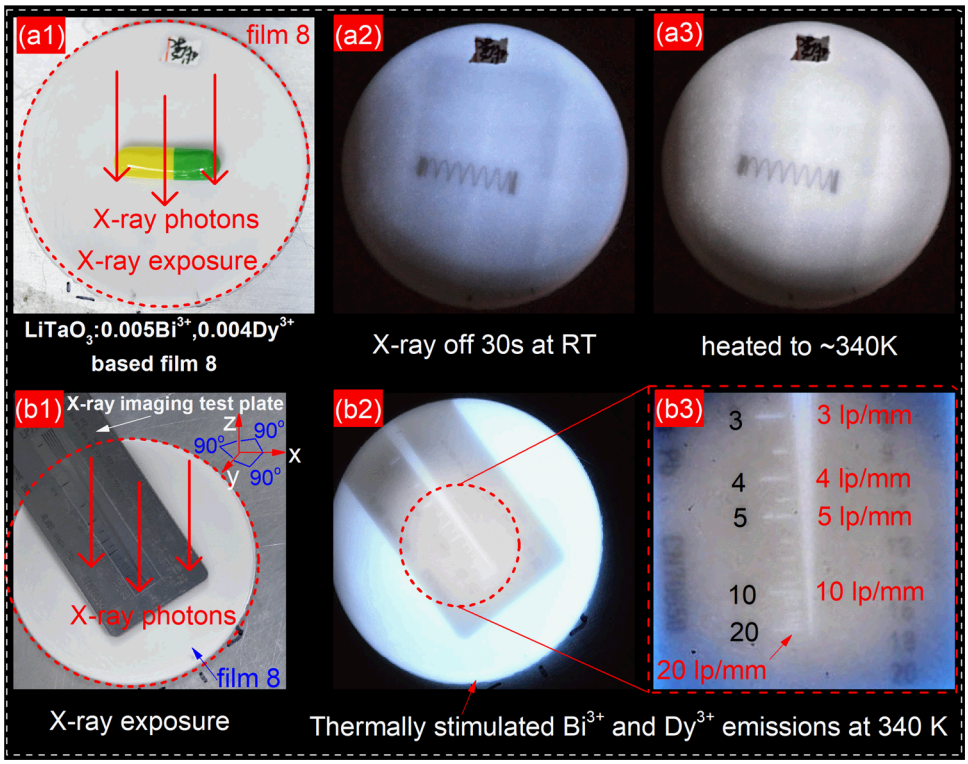

Figure 11. Illustration of X-ray detection by X-ray imaging. a1) until a3) Proof-of-concept X-ray imaging by using a2) Bi^{3+} and Dy^{3+} afterglow and b3) thermally stimulated Bi^{3+} and Dy^{3+} emissions from $LiTaO_3$:0.005Bi^{3+},0.004Dy^{3+} in the film 8. b1) until b3) X-ray imaging resolution test of $LiTaO_3$:0.005Bi^{3+},0.004Dy^{3+}-based film 8.

$LiTaO_3$:0.005Bi^{3+},0.002Dy^{3+} in Figure 10d3. The thermally stimulated emission color can be tailored from white to slight yellow by heating the sample from RT to ≈373 K in Figure 10d3,d4, demonstrating the potential application in anticounterfeiting. After bleaching at ≈373 K, the text of "WX" is not visible in both the dark and daylight as in Figure 10d5. In addition to thermal stimulation in Figure 10d5, information erasure by optical stimulation has been explored in $LiTaO_3$:0.005Bi^{3+},0.002Dy^{3+}-based film by different energy photon stimulation of WLED in Figure 10e1–e3, and 656 nm laser in Figure 10f1–f3. 2D information storage, display, and erasure have also been demonstrated in the $LiTaO_3$:0.005Bi^{3+},0.002Dy^{3+}-based film 1 in Figure S24 (Supporting Information). Information storage and display applications are also explored by using the $LiTaO_3$:0.002Bi^{3+},0.004Dy^{3+}-based 3D films 2–7 as demonstrated in Figure S25 (Supporting Information).

To further demonstrate the detection of X-rays, we made an X-ray imaging film, named film 8, by dispersing $LiTaO_3$:0.005Bi^{3+},0.004Dy^{3+} in silica gel as shown in **Figure 11**a1. A capsule with metal spring was used as the object for X-ray detection. Two white X-ray imaging photographs were obtained by thermally stimulated Bi^{3+} and Dy^{3+} emissions in $LiTaO_3$:0.005Bi^{3+}, 0.004Dy^{3+} at RT in Figure 11a2 and at ≈340 K in Figure 11a3 in the dark. We have verified the X-ray imaging resolution for film 8 in Figure 11b1. Film 8 was placed underneath a Pb-based X-ray imaging test plate, which has Pb-free scale marks from 0 to 20 lp mm^{-1}. Both the imaging test plate and film 8 on a table were exposed in the dark to X-rays under perpendicular incidence as illustrated in Figure 11b1. The traps in $LiTaO_3$:0.005Bi^{3+},0.004Dy^{3+} in film 8 were filled by X-ray charging. An intense white photograph appears in Figure 11b2 because of the thermally stimulated Bi^{3+} and Dy^{3+} emissions at ≈340 K. From the circular region in Figure 11b2, an X-ray imaging resolution of ≈20 lp mm^{-1} is estimated in Figure 11b3. The results in Figures 9–11 demonstrate that the developed $LiTaO_3$:$x$$Bi^{3+}$,$y$$Dy^{3+}$ phosphors can be used as light-sensing materials for developing new photodetectors that can detect a wide energy range of photons from X-rays to 850 nm infrared light.

4. Discussion

4.1. VRBEs in the Bi^{3+} and Bi^{2+} Ground States in $LiTaO_3$

To understand the charge-carrier capturing and release processes in $LiTaO_3$:$x$$Bi^{3+}$,$y$$Dy^{3+}$, the VRBEs in the ground states of Bi^{2+} and Bi^{3+} are crucial. In general, Bi^{3+} has the most stable electronic configuration of $[Xe]4f^{14}5d^{10}6s^2$ in an inorganic compound.[31] During exposure to high-energy radiation like X-rays, γ-rays or also often 254 nm UV light, free mobile electrons and/or holes are generated in a compound. When both the VRBEs in the Bi^{2+} ground state and in the Bi^{3+} ground state are located in the forbidden band of the compound, Bi^{3+} can act as both an electron-trapping center and a hole-trapping center.[32] Such a dual role of Bi^{3+} has been evidenced in $LnPO_4$ (Ln = La,

Y, or Lu) and $NaYGeO_4$ in refs. [16, 25]. The VRBE in the $^2P_{1/2}$ ground state of Bi^{2+} in 15 different compounds has been studied in ref. [33], and it falls in the range near -3.5 ± 0.5 eV. We therefore expect that there is a Bi^{2+} $^2P_{1/2}$ ground state with a VRBE value of -3.5 ± 0.5 eV in $LiTaO_3$ in Figure 1. Figure 1 then predicts that Bi^{3+} could act as an $\approx 0.8 \pm 0.5$ eV deep electron-capturing center in $LiTaO_3$.

To determine the VRBEs in the ground and excited states of Bi^{3+}, the spectroscopy of Bi^{3+}-doped $LiTaO_3$ needs to be studied as in Figure 4a,b. Bi^{3+} has $[Xe]4f^{14}5d^{10}6s^16p^1$ as the lowest energy excited configuration.[34] Bi^{3+} excitation bands originate from the electron transitions from the Bi^{3+} $^1S_0$ ground state to the $^3P_1$, $^3P_2$, and $^1P_1$ excited states, which are generally known as the Bi^{3+} A, B, and C bands.[35] In addition, often a broad Bi^{3+} excitation band emerges, denoted as the Bi^{3+} D band, which is attributed to the electron transfer from Bi^{3+} to the conduction band (CB) of a compound.[34,36] The Bi^{3+} B band is a spin-forbidden transition, and its intensity is very weak and usually not observed. The Bi^{3+} C band is a spin-allowed transition,[16] and there is an empirical formula for the energy relation between the Bi^{3+} C band (E_{BiC}) and the A band (E_A) in inorganic compounds by Equation (3)[37]

$$E_{BiC} = 3.236 + 2.290 \times (E_A - 2.972)^{0.856} \quad (3)$$

Figure 4b shows that the excitation spectrum ($\lambda_{em} = 583$ nm) in the 200–350 nm region of $LiTaO_3$:$0.005Bi^{3+}$,$0.005Dy^{3+}$ can be fitted by a narrow band peaked at ≈243 nm, a broad band peaked near 278 nm, and a band peaked at 300 nm. Like in ref. [24], the excitation band peaked at 300 nm is assigned to the Bi^{3+} A band.[38] Considering the large Stokes shift and broadband nature, the broad emission band peaked near 438 nm in Figure 4b is assigned to Bi^{3+} D-band emission. With $E_A = 4.13$ eV (300 nm), the Bi^{3+} C band is predicted by Equation (3) to ≈212 nm (5.84 eV), which is higher than the bandgap energy. The narrow excitation peak at 243 nm is then not assigned to the C band but tentatively to intrinsic defect(s) in $LiTaO_3$. Because the excitation band peaked near 278 nm in Figure 4b is broad and the $LiTaO_3$:$0.005Bi^{3+}$,$0.004Dy^{3+}$ phosphor can be charged by optical excitation with this broadband in Figure 7b, we assign the excitation band peaked near 278 nm to the Bi^{3+} D band. Based on the Bi^{3+} A- and D-band energies, the VRBEs in the $^1S_0$ ground state and $^3P_1$ excited state of Bi^{3+} in $LiTaO_3$ are determined to be −7.16 and −3.03 eV, as illustrated in Figure 1. This implies that the phosphor can be charged by both A- and D-band excitations, which are consistent with the TL excitation plot for $LiTaO_3$:$0.005Bi^{3+}$,$0.004Dy^{3+}$ in Figure 7b. The Bi^{3+} $^3P_1$ excited state is very close to the conduction band bottom and upon excitation the electron from $^3P_1$ may delocalize to arrive at a situation similar to D-band excitation. Figure 1 predicts that Bi^{3+} can act as a ≈1.3 eV deep hole-capturing center.

4.2. Charge-Carrier Trapping and Detrapping Processes in $LiTaO_3$:xBi^{3+},yDy^{3+}

Figure 1 shows that the ground states of Dy^{3+} and Dy^{2+} are in the valence band and the conduction band. It means that Dy^{3+} cannot act as an electron- or a hole-capturing center in $LiTaO_3$. Figure 4a,b,e shows that the intrinsic defect(s) excitation band at ≈243 nm, Bi^{3+} D and A bands peaked near ≈278 and ≈300 nm appear in the excitation spectra of $LiTaO_3$:$0.005Bi^{3+}$,yDy^{3+} when the Dy^{3+} typical ≈580 nm emission is monitored. This implies that, upon excitation, there are energy-transfer processes from both the intrinsic defect(s) and Bi^{3+} to Dy^{3+}, leading to the characteristic Dy^{3+} 4f → 4f emissions in Figure 4b–d. The energy transfer from Bi^{3+} to Dy^{3+} also generates the Dy^{3+} emission in the thermally stimulated luminescence spectra of $LiTaO_3$:$0.005Bi^{3+}$,yDy^{3+} ($y = 0.004$ or 0.006) in Figure 5a,b and in the afterglow spectra of $LiTaO_3$:$0.002Bi^{3+}$,$0.004Dy^{3+}$ in Figure 5c. One role of Dy^{3+} co-doping in $LiTaO_3$:xBi^{3+},yDy^{3+} is then to obtain Dy^{3+} 4f → 4f emissions to generate Dy^{3+}- and Bi^{3+}-based white afterglows, as demonstrated in Figures 3c3, 6f, and 11. The other role of Dy^{3+} co-doping might be to induce and optimize the formation of defect(s) in $LiTaO_3$:xBi^{3+},yDy^{3+} to optimize the photochromic phenomenon for light-sensing application, as shown in Figures 3, 6d, 8, and 10 and in Figures S24 and S25 (Supporting Information). An intense TL glow peak near 322 K appears in >100 K TLEM spectrum of $LiTaO_3$:$0.005Bi^{3+}$,$0.006Dy^{3+}$ in Figure 5a. Assuming a first-order TL-recombination kinetics, its trap depth can be estimated to be ≈0.89 eV by using Equation (1) with $T_m = 322$ K, $\beta = 0.2$ K s^{-1}, and $s = 1.80 \times 10^{12}$ s^{-1}. This value is within the predicted trap depth range of ≈0.8 ± 0.5 eV for Bi^{3+} electron-trapping center in $LiTaO_3$ in Figure 1. Considering that Bi^{3+} can act as an ≈1.3 eV deep hole-trapping center in Figure 1, the 322 K TL peak may be due to electron liberation from Bi^{2+} and recombination with the hole at Bi^{4+} to produce the Bi^{3+} D-band emission. More work is needed to further testify this mechanism. The 322 K TL peak can also be attributed to electron release from $LiTaO_3$ host defect(s) and recombination with the hole at Bi^{4+} to yield Bi^{3+} D-band emission. The same applies to the TL glow peaks near ≈323–340 and ≈392 K in $LiTaO_3$:$0.005Bi^{3+}$,yDy^{3+} in Figure 6b. The TL peak near ≈341–360 K in $LiTaO_3$:$0.005Bi^{3+}$,yDy^{3+} ($y = 0.0005$–0.004) charged by 254 nm UV light in Figure 6d is about 20 K higher that in Figure 6b when X-rays are used as the charging light source. A possible reason is that the trap with a trap depth distribution in $LiTaO_3$:$0.005Bi^{3+}$,yDy^{3+}, as evidenced in Figure S15 (Supporting Information), can be filled differently after exposure to X-rays or 254 nm UV light. For UV-light-charging processes in Figure 7, mobile charge carriers are created via the efficient photoinduced ionization processes from the Bi^{3+} excitation A or D band in $LiTaO_3$:$0.005Bi^{3+}$,yDy^{3+}.[39] Figure 6d shows that the TL intensity after UV illumination is 10 000 times stronger than with X-ray excitation in Figure 6b. With X-rays, traps may be partly filled and, with UV, some traps may be completely filled (saturated) and contribute less to the overall TL glow. This may cause that the glow appears differently.

Figure 9b–e demonstrates that the stored charge carriers in $LiTaO_3$:$0.005Bi^{3+}$, $0.001Dy^{3+}$ and $LiTaO_3$:$0.005Bi^{3+}$,$0.004Dy^{3+}$ can be optically stimulated to obtain Bi^{3+} and Dy^{3+} emissions by different energy photon from 365 nm (≈3.4 eV) UV light to 850 nm laser (≈1.46 eV). The photon energy from 1.46 and 3.4 eV is much larger than the deepest electron trap depth of ≈1.04 eV and the Bi^{3+} hole trap depth of ≈1.3 eV in $LiTaO_3$:$0.005Bi^{3+}$, $0.001Dy^{3+}$, as illustrated in Figures 1 and 6b. It means that the photon energy is high enough to optically stimulate the electron captured at traps corresponding with the TL glow curve from ≈305 to ≈450 K to become a free mo-

bile electron in the conduction band. The electron can then recombine with a hole trapped at Bi^{4+} to generate the Bi^{3+} emission and characteristic Dy^{3+} 4f → 4f emissions via energy transfer from Bi^{3+} to Dy^{3+} in $LiTaO_3$:0.005Bi^{3+},0.001Dy^{3+}. Figures 8 and 9c show that there is a linear relation between the reversible photochromic phenomenon and the stored charge carriers in $LiTaO_3$:0.005Bi^{3+}, 0.001Dy^{3+}. It is also unique that the photochromic $LiTaO_3$:0.005Bi^{3+}, 0.001Dy^{3+} phosphor can be bleached by heating at 450 K in Figure 10d5, or by a wide photon energy stimulation from 365 nm UV light to 850 nm infrared light in Figure 9. One may use this feature of optically induced photochromism to explore information storage and read-out applications like in Figure 10 and in Figures S24 and S25 (Supporting Information).

5. Conclusions

We have combined the spectroscopy, thermoluminescence, and VRBE construction to unravel the trapping and release processes of charge carriers in $LiTaO_3$:$x$$Bi^{3+}$,$y$$Dy^{3+}$. The photoluminescence excitation and emission spectra of $LiTaO_3$:0.005Bi^{3+},0.005Dy^{3+} were first analyzed at RT and 10 K. Upon excitation of Bi^{3+}, the energy transfer processes from Bi^{3+} to Dy^{3+} are identified, leading to characteristic Dy^{3+} 4f → 4f emissions. The excitation bands peaked at near 243, 278, and 300 nm are assigned to intrinsic defect(s), Bi^{3+} excitation D and A bands in $LiTaO_3$. The VRBEs in the $^1S_0$ ground and $^3P_1$ excited states of Bi^{3+} in $LiTaO_3$ were determined to be −7.16 and −3.03 eV by using the energies of the Bi^{3+} excitation D and A bands. The VRBE in the Bi^{2+} $^2P_{1/2}$ ground state in $LiTaO_3$ is roughly estimated to be about −3.5 ± 0.5 eV, which needs to further be studied. Bi^{3+} appears to act as an ≈1.3 eV deep hole-trapping center and maybe as a 0.80±0.5 eV deep electron-trapping center. Upon charging $LiTaO_3$:$x$$Bi^{3+}$,$y$$Dy^{3+}$, electrons are trapped at host intrinsic defects and holes are trapped at Bi^{4+}. Electron detrapping and recombination with hole trapped at Bi^{4+} generates Bi^{3+} luminescence. Dy^{3+} cation does not act as a charge carrier capturing center, but acts as a luminescence center via energy transfer processes of Bi^{3+} → Dy^{3+} to generate Dy^{3+} characteristic 4f → 4f emissions in $LiTaO_3$:$x$$Bi^{3+}$,$y$$Dy^{3+}$. More than 3 or 40 h of Bi^{3+}- and Dy^{3+}-based white afterglow is measurable in $LiTaO_3$:0.005Bi^{3+}, 0.004Dy^{3+} after exposure to X-rays or 254 nm UV light. A linear relation between the amount of stored charge carriers and the photochromic phenomenon appears in $LiTaO_3$:$x$$Bi^{3+}$,$y$$Dy^{3+}$. The charge carriers can be stored in $LiTaO_3$:$x$$Bi^{3+}$,$y$$Dy^{3+}$ by X-rays or 254 nm UV-light charging. The stored charge carriers can be removed by heating or with an optically stimulated Bi^{3+} and Dy^{3+} emission process by a wide energy photon stimulation, i.e., from 365 nm UV light to 850 nm infrared laser. Proof-of-concept light detection applications like 2D information storage and anticounterfeiting or X-ray imaging were demonstrated by using the photochromic and white afterglow $LiTaO_3$:$x$$Bi^{3+}$,$y$$Dy^{3+}$ phosphors. This work not only promotes our understanding on the VRBEs and the level locations of Bi^{2+} and Bi^{3+}, and the charge-carrier trapping processes in $LiTaO_3$:$x$$Bi^{3+}$,$y$$Dy^{3+}$, but also can accelerate the development of optical material that can detect a wide energy photon from X-rays to infrared light for photodetector applications.

Supporting Information

Supporting Information is available from the Wiley Online Library or from the author.

Acknowledgements

T.L. acknowledged the financial supports from the National Natural Science Foundation of China (Grant No. 12104170), the Fundamental Research Funds for the Central Universities (No. ZQN-1023), the Scientific Research Funds of Huaqiao University (Grant No. 21BS106), and the measurement supports from the Instrumental Analysis Center of Huaqiao University.

Conflict of Interest

The authors declare no conflict of interest.

Data Availability Statement

The data that support the findings of this study are available on request from the corresponding author. The data are not publicly available due to privacy or ethical restrictions.

Keywords

bismuth, information storage and X-ray imaging, $LiTaO_3$ perovskite, photochromic phenomena, white persistent luminescence

Received: January 26, 2022
Revised: May 13, 2022
Published online:

[1] Z. Yang, J. Du, L. I. D. J. Martin, D. Van der Heggen, D. Poelman, *Laser Photonics Rev.* **2021**, *15*, 2000525.
[2] Z. Yang, J. Du, L. I. D. J. Martin, A. Feng, E. Cosaert, B. Zhao, W. Liu, R. Van Deun, H. Vrielinck, D. Poelman, *Adv. Opt. Mater.* **2021**, *9*, 2100669.
[3] Z. Hu, X. Huang, Z. Yang, J. Qiu, Z. Song, J. Zhang, G. Dong, *Light: Sci. Appl.* **2021**, *10*, 140.
[4] Y. Ren, Z. Yang, M. Li, J. Ruan, J. Zhao, J. Qiu, Z. Song, D. Zhou, *Adv. Opt. Mater.* **2019**, *7*, 1900213.
[5] C.-T. Poon, W. H. Lam, V. W.-W. Yam, *J. Am. Chem. Soc.* **2011**, *133*, 19622.
[6] J. Ruan, Z. Yang, Y. Wen, M. Li, Y. Ren, J. Qiu, Z. Song, Y. Wang, *Chem. Eng. J.* **2020**, *383*, 123180.
[7] X. Bai, Z. Yang, Y. Zhan, Z. Hu, Y. Ren, M. Li, Z. Xu, A. Ullah, I. Khan, J. Qiu, Z. Song, B. Liu, Y. Wang, *ACS Appl. Mater. Interfaces* **2020**, *12*, 21936.
[8] X. Bai, Y. Cun, Z. Xu, Y. Zi, A. A. Haider, A. Ullah, I. Khan, J. Qiu, Z. Song, Z. Yang, *Chem. Eng. J.* **2022**, *429*, 132333.
[9] Z. Yang, J. Hu, L. I. D. J. Martin, D. Van der Heggen, D. Poelman, *J. Mater. Chem. C* **2021**, *9*, 14012.
[10] M. Akiyama, *Appl. Phys. Lett.* **2010**, *97*, 181905.
[11] U. Joost, A. Šutka, M. Oja, K. Smits, N. Döbelin, A. Loot, M. Järvekülg, M. Hirsimäki, M. Valden, E. Nõmmiste, *Chem. Mater.* **2018**, *30*, 8968.
[12] S. Wang, W. Fan, Z. Liu, A. Yu, X. Jiang, *J. Mater. Chem. C* **2018**, *6*, 191.
[13] Q. Jia, Q. Zhang, H. Sun, X. Hao, *J. Eur. Ceram. Soc.* **2021**, *41*, 1211.
[14] Y.-M. Yang, Z.-Y. Li, J.-Y. Zhang, Y. Lu, S.-Q. Guo, Q. Zhao, X. Wang, Z.-J. Yong, H. Li, J.-P. Ma, Y. Kuroiwa, C. Moriyoshi, L.-L. Hu, L.-Y. Zhang, L.-R. Zheng, H.-T. Sun, *Light: Sci. Appl.* **2018**, *7*, 88.

[15] D. Van der Heggen, R. Zilenaite, E. Ezerskyte, V. Fritz, K. Korthout, D. Vandenberghe, J. De Grave, J. Garrevoet, L. Vincze, D. Poelman, J. J. Joos, P. F. Smet, *Adv. Funct. Mater.* **2022**, *32*, 2109635.
[16] T. Lyu, P. Dorenbos, *Chem. Mater.* **2020**, *32*, 1192.
[17] J. Xu, S. Tanabe, *J. Lumin.* **2019**, *205*, 581.
[18] S. Zhang, Z. Song, S. Wang, Z. Wang, F. Wang, Q. Liu, *J. Mater. Chem. C* **2020**, *8*, 4956.
[19] J. Ueda, S. Miyano, J. Xu, P. Dorenbos, S. Tanabe, *Adv. Photonics Res.* **2021**, *2*, 2000102.
[20] a) H. Yuan, R. Génois, E. Glais, F. Chen, Q. Shen, L. Zhang, E. Faulques, L. Qi, F. Massuyeau, R. Gautier, *Matter* **2021**, *4*, 3967; b) Y. Wang, H. Guo, *Front. Chem.* **2021**, *9*.
[21] Z. Gong, W. Zheng, Y. Gao, P. Huang, D. Tu, R. Li, J. Wei, W. Zhang, Y. Zhang, X. Chen, *Angew. Chem., Int. Ed.* **2019**, *58*, 6943.
[22] M. Grinberg, J. Barzowska, Y. Shen, K. L. Bray, *Phys. Rev. B* **2001**, *63*, 214104.
[23] M. Nikl, R. Morlotti, C. Magro, R. Bracco, *J. Appl. Phys.* **1996**, *79*, 2853.
[24] R. Hu, Y. Zhang, Y. Zhao, X. Wang, G. Li, C. Wang, *Chem. Eng. J.* **2020**, *392*, 124807.
[25] T. Lyu, P. Dorenbos, *J. Mater. Chem. C* **2018**, *6*, 6240.
[26] T. Lyu, P. Dorenbos, *Laser Photonics Rev.* **2022**, https://doi.org/10.1002/lpor.202200304
[27] A. J. J. Bos, R. M. van Duijvenvoorde, E. van der Kolk, W. Drozdowski, P. Dorenbos, *J. Lumin.* **2011**, *131*, 1465.
[28] a) Z. Lu, W. Zhang, J. Chen, S. Chen, J. Cao, H. Guo, *J. Lumin.* **2021**, *232*, 117857; b) F. Kang, Y. Zhang, M. Peng, *Inorg. Chem.* **2015**, *54*, 1462.
[29] a) W. Hoogenstraaten, *Philips Res. Rep* **1958**, *13*, 515; b) J. Azorín, *Int. J. Rad. Appl. Instrum. D* **1986**, *11*, 159.
[30] K. Van den Eeckhout, A. J. J. Bos, D. Poelman, P. F. Smet, *Phys. Rev. B* **2013**, *87*, 045126.
[31] B. Lou, J. Wen, L. Ning, M. Yin, C.-G. Ma, C.-K. Duan, *Phys. Rev. B* **2021**, *104*, 115101.
[32] a) R. H. P. Awater, P. Dorenbos, *J. Phys. Chem. C* **2016**, *120*, 15114; b) P. Dorenbos, *ECS J. Solid State Sci. Technol.* **2021**, *10*, 086002.
[33] R. H. P. Awater, P. Dorenbos, *J. Lumin.* **2017**, *188*, 487.
[34] R. H. P. Awater, P. Dorenbos, *J. Lumin.* **2017**, *184*, 221.
[35] P. Boutinaud, *Inorg. Chem.* **2013**, *52*, 6028.
[36] a) P. Dorenbos, *Opt. Mater.* **2017**, *69*, 8; b) P. Boutinaud, E. Cavalli, *Chem. Phys. Lett.* **2011**, *503*, 239; c) H. C. Swart, R. E. Kroon, *Opt. Mater.: X* **2019**, *2*, 100025.
[37] L. Wang, Q. Sun, Q. Liu, J. Shi, *J. Solid State Chem.* **2012**, *191*, 142.
[38] H. Cai, Z. Song, Q. Liu, *Mater. Chem. Front.* **2021**, *5*, 1468.
[39] J. Ueda, P. Dorenbos, A. J. J. Bos, A. Meijerink, S. Tanabe, *J. Phys. Chem. C* **2015**, *119*, 25003.